









# Engineering the Cu/Mo<sub>2</sub>CT<sub>x</sub> (MXene) interface to drive CO<sub>2</sub> hydrogenation to methanol

## Journal Article

### Author(s):

Zhou, Hui; [Chen, Zixuan](#) ; Vidal López, Anna; Díaz López, Estefanía; Lam, Erwin; Tsoukalou, Athanasia; Willinger, Elena; Kuznetsov, Denis ; Mance, Deni; Kierzkowska-Stürzlinger, Agnieszka ; Donat, Felix ; Abdala, Paula Macarena ; Comas Vives, Aleix ; Copéret, Christophe ; Fedorov, Alexey ; Müller, Christoph R.

### Publication date:

2021-10

### Permanent link:

<https://doi.org/10.3929/ethz-b-000512844>

### Rights / license:

[Creative Commons Attribution 4.0 International](#)

### Originally published in:

Nature Catalysis 4(10), <https://doi.org/10.1038/s41929-021-00684-0>

### Funding acknowledgement:

800419 - Sorbent-enhanced Steam Biomass Reforming for Integrated Bio-energy with Carbon Capture and (EC)

819573 - Advancing CO<sub>2</sub> Capture Materials by Atomic Scale Design: the Quest for Understanding (EC)

ETH-40 17-2 - Advanced materials by atomic layer deposition (ALD): from controlling porosity of ALD-grown overcoats to the molecular understanding of silica-aluminas (ETHZ)

ETH-44 16-2 - The direct integration of CO<sub>2</sub> conversion into CO<sub>2</sub> capture: Development of model bi-functional Cu-MgO-MO<sub>x</sub> materials through the elucidation of the carbonation mechanism and active sites for CO<sub>2</sub> hydrogenation (ETHZ)

# Engineering the Cu/Mo<sub>2</sub>CT<sub>x</sub> (MXene) Interface to Drive CO<sub>2</sub> Hydrogenation to Methanol

Hui Zhou,<sup>1</sup> Zixuan Chen,<sup>1</sup> Anna Vidal López,<sup>2</sup> Estefanía Díaz López,<sup>2</sup> Erwin Lam,<sup>3</sup> Athanasia Tsoukalou,<sup>1</sup> Elena Willinger,<sup>1</sup> Denis A. Kuznetsov,<sup>1</sup> Deni Mance,<sup>3</sup> Agnieszka Kierzkowska,<sup>1</sup> Felix Donat,<sup>1</sup> Paula M. Abdala,<sup>1</sup> Aleix Comas-Vives,<sup>2\*</sup> Christophe Copéret,<sup>3\*</sup> Alexey Fedorov,<sup>1\*</sup> and Christoph R. Müller<sup>1\*</sup>

\*Corresponding author. Email: Aleix.Comas@uab.cat; ccoperet@ethz.ch; fedoroal@ethz.ch; muelchri@ethz.ch

**Affiliations** <sup>1</sup>Department of Mechanical and Process Engineering, ETH Zürich, CH-8092 Zürich, Switzerland. <sup>2</sup>Department of Chemistry, Autonomous University of Barcelona, 08193 Cerdanyola del Valles, Catalonia, Spain. <sup>3</sup>Department of Chemistry and Applied Biosciences, ETH Zürich, CH-8093 Zürich, Switzerland.

## Abstract

Development of efficient catalysts for the direct hydrogenation of CO<sub>2</sub> to methanol is essential for the valorization of this abundant feedstock. Here we show that a silica-supported Cu/Mo<sub>2</sub>CT<sub>x</sub> (MXene) catalyst achieves a higher intrinsic methanol formation rate per mass Cu than the reference Cu/SiO<sub>2</sub> catalyst with a similar Cu loading. The Cu/Mo<sub>2</sub>CT<sub>x</sub> interface can be engineered owing to the higher affinity of metallic Cu for the partially reduced MXene surface (in preference to the SiO<sub>2</sub> surface) and the mobility of Cu under H<sub>2</sub> at 500 °C.

Increasing the reduction time, the Cu/Mo<sub>2</sub>CT<sub>x</sub> interface becomes more Lewis acidic due to the higher amount of Cu<sup>+</sup> sites dispersed onto the reduced Mo<sub>2</sub>CT<sub>x</sub> and this correlates with an

increased rate of CO<sub>2</sub> hydrogenation to methanol. The critical role of the interface between Cu and Mo<sub>2</sub>CT<sub>x</sub> is further highlighted by DFT calculations that identify formate and methoxy species as stable reaction intermediates.

## Introduction

Carbon dioxide, a major contributor to climate change, is potentially an abundant carbon resource for chemicals and fuels. Among the different approaches for CO<sub>2</sub> conversion, the direct catalytic hydrogenation of CO<sub>2</sub> to methanol is an emerging technology for decreasing CO<sub>2</sub> emissions and storing renewable hydrogen obtained from intermittent solar or wind energy, forming thereby the basis of the methanol economy<sup>1,2</sup>. While the industrial Cu-based methanol synthesis catalyst, Cu-ZnO-Al<sub>2</sub>O<sub>3</sub><sup>3,4</sup>, is efficient in converting a mixture of H<sub>2</sub>, CO and CO<sub>2</sub> (i.e. synthesis gas) to methanol, this catalyst has generally been considered to be less efficient with CO<sub>2</sub>-rich feeds, especially at lower space velocities,<sup>3,5-10</sup> although there is some counter evidence<sup>11</sup>. By using specific supports, e.g. Cu/ZrO<sub>2</sub><sup>12-14</sup>, the catalytic performance of Cu-based catalysts for the direct CO<sub>2</sub> hydrogenation to methanol can be improved; however, the activity and selectivity of these catalysts are currently insufficient for their industrial deployment. A complementary counterexample is Cu on reducible supports such as TiO<sub>2</sub> or CeO<sub>2</sub>, that mostly leads to the formation of CO via the reverse water-gas shift reaction (RWGS) resulting in low production rates of methanol<sup>14-16</sup>. Overall, the nature of the support and the Cu-support interface are essential parameters for controlling the catalyst performance<sup>17-19</sup>. For instance, the introduction of isolated Ti(IV) and Zr(IV) surface sites to Cu/SiO<sub>2</sub>, which itself is a poor methanol synthesis catalyst, significantly improves its activity and selectivity, making it on par with Cu/ZrO<sub>2</sub><sup>13,15</sup>.

In contrast to reducible oxides that are prone to strong metal-support interaction (SMSI), leading to the overcoating of metal particles with a reduced support, i.e. a geometric effect),

transition-metal carbides feature electronic metal-support interactions<sup>20–24</sup>. MXene materials, i.e. a family of two-dimensional (2D) carbides, nitrides, and carbonitrides<sup>25–27</sup> with the general formula of  $M_{n+1}X_nT_x$  (where M is an early transition metal,  $n = 1, 2, 3$ , X is C and/or N, and T are surface  $-O-$ ,  $-OH$ , and/or  $-F$  groups), are currently emerging in thermocatalytic applications as catalysts<sup>28–30</sup> or supports with reactive metal-support interactions<sup>31–34</sup>. MXenes without surface termination groups are oxophilic and therefore bind and activate  $CO_2$  strongly<sup>35</sup>.

Here we report that silica-supported, dispersed, reducible nanosheets of a delaminated molybdenum MXene,  $Mo_2CT_x$ , can be used to engineer a  $Cu/Mo_2CT_x$  interface that shows a ca. six times increased copper-normalized intrinsic formation rate of methanol by the direct hydrogenation of  $CO_2$  as compared to  $Cu/SiO_2$ , and a higher selectivity to methanol at higher  $CO_2$  conversions (ca. 37% at  $X(CO_2) = 3.2\%$  under 25 bar). To develop this silica-supported catalyst ( $Cu/Mo_2CT_x/SiO_2$ ), we rely on surface organometallic chemistry (SOMC),<sup>36</sup> to graft a copper mesityl precursor onto  $Mo_2CT_x/SiO_2$ . Treatment of the grafted material in  $H_2$  leads to the migration of Cu from the silica surface onto the  $Mo_2CT_x$  nanosheets. *Operando* diffuse reflectance infrared Fourier transform spectroscopy (DRIFTS) and solid-state nuclear magnetic resonance (ssNMR) using  $^{13}C$ -labelled  $CO_2$  and  $H_2$  indicate the presence of surface formate and methoxy intermediates at the  $Cu/Mo_2CT_x$  interface in higher abundance as compared to the reference  $Cu/SiO_2$  interface, correlating directly with the higher catalytic activity of  $Cu/Mo_2CT_x/SiO_2$ , which is further confirmed by density functional theory (DFT) calculations. Finally, Cu  $L_3VV$  Auger spectra and DRIFTS data using CO as a probe molecule indicate that the increased catalytic activity of  $Cu/Mo_2CT_x/SiO_2$  is associated with a higher fraction of Lewis acidic  $Cu^+$  sites at the  $Cu/Mo_2CT_x$  interface, which is supported by DFT calculations.

## Results

### Synthesis and characterization of Cu/Mo<sub>2</sub>CT<sub>x</sub>/SiO<sub>2</sub>

Delaminated atomically thin nanosheets of Mo<sub>2</sub>CT<sub>x</sub> were dispersed from a colloidal solution (Supplementary Figure 1) onto a silica support, using incipient wetness impregnation according to a previously reported method developed in our group<sup>30</sup>. The resulting Mo<sub>2</sub>CT<sub>x</sub>/SiO<sub>2</sub> material (0.3 wt% Mo loading, Fig. 1a and Supplementary Figure 2) was then dehydroxylated at 500 °C under N<sub>2</sub> flow, yielding Mo<sub>2</sub>CT<sub>x</sub>/SiO<sub>2-500</sub> with 0.47 mmol g<sup>-1</sup> of ≡SiOH sites according to titration with dibenzyl magnesium. The dehydroxylation of the silica surface does not affect the integrity of the supported Mo<sub>2</sub>CT<sub>x</sub> nanosheets, at least up to 800 °C as previously reported<sup>30</sup>. We then grafted [Cu<sub>n</sub>(Mesityl)<sub>n</sub>, n = 2, 4, 5, (CuMes)] onto Mo<sub>2</sub>CT<sub>x</sub>/SiO<sub>2-500</sub> in toluene using 0.83 equiv. of Cu per silanol site. The infrared (IR) spectrum of the grafted material shows the consumption of the isolated ≡SiOH band at 3745 cm<sup>-1</sup> and the appearance of new C–H bands at 3019, 2925, 2868, and 1597 cm<sup>-1</sup> (Fig. 1b), indicating the successful grafting of CuMes on ≡SiOH sites<sup>15,37</sup>. Treatment under H<sub>2</sub> at 500 °C for 2 h restored the ≡SiOH groups while C–H stretching bands disappeared (Fig. 1b) due to the complete hydrogenolysis of the grafted CuMes precursor in this material, denoted Cu/Mo<sub>2</sub>CT<sub>x</sub>/SiO<sub>2-2h</sub> (the time of the H<sub>2</sub> treatment is indicated in the subscript notation). Increasing the time of the H<sub>2</sub> reduction to 6 h gave the Cu/Mo<sub>2</sub>CT<sub>x</sub>/SiO<sub>2-6h</sub> material. We also prepared silica-supported Cu nanoparticles via the same approach using CuMes as a precursor (i.e. reference Cu/SiO<sub>2-2h</sub> catalyst), as previously reported<sup>17,36,37</sup>. In what follows, we contrast the nature of the Cu/support interface with the performance of Cu/SiO<sub>2-2h</sub>, Cu/Mo<sub>2</sub>CT<sub>x</sub>/SiO<sub>2-2h</sub>, Cu/Mo<sub>2</sub>CT<sub>x</sub>/SiO<sub>2-6h</sub> as well as the industrial Cu-ZnO-Al<sub>2</sub>O<sub>3</sub> benchmark for the hydrogenation of CO<sub>2</sub> to methanol.

High-angle annular dark-field scanning transmission electron microscopy imaging (HAADF-STEM) shows small Cu nanoparticles (NPs) with a narrow size distribution ( $2.9 \pm 0.4$  nm) on the SiO<sub>2</sub> surface, for both Cu/Mo<sub>2</sub>CT<sub>x</sub>/SiO<sub>2</sub> materials and for the Cu/SiO<sub>2-2h</sub> reference material (unless specified otherwise, specimens were exposed to ambient air prior to analysis with transmission electron microscopy (TEM), Supplementary Figure 3). The Cu loadings, as determined by inductively coupled plasma (ICP) analysis, are similar in the catalysts, i.e. 2.4 and 2.0 wt% Cu for Cu/Mo<sub>2</sub>CT<sub>x</sub>/SiO<sub>2-2h</sub> and Cu/SiO<sub>2-2h</sub>, respectively. Energy-dispersive X-ray spectroscopy (EDX) of two distinct areas in Cu/Mo<sub>2</sub>CT<sub>x</sub>/SiO<sub>2-2h</sub> confirms that Cu is dispersed on both SiO<sub>2</sub> and Mo<sub>2</sub>CT<sub>x</sub> (Regions 1 and 2, respectively, in Fig. 1c). Interestingly, the intensity of the Cu signal (normalized by the Si signal) on Mo<sub>2</sub>CT<sub>x</sub> (Region 2) is 3.2 times higher than that on SiO<sub>2</sub> (Region 1), indicating that Cu is enriched on the Mo<sub>2</sub>CT<sub>x</sub> phase in preference to SiO<sub>2</sub>. Performing a similar analysis of the intensities of the Cu signal in CuMes/Mo<sub>2</sub>CT<sub>x</sub>/SiO<sub>2</sub> (i.e. the material prior to H<sub>2</sub> reduction) shows that Cu is dispersed uniformly on Mo<sub>2</sub>CT<sub>x</sub> and SiO<sub>2</sub> (Supplementary Figure 4). These results indicate the mobility of Cu during the H<sub>2</sub> treatment at 500 °C and the preferential migration of Cu from SiO<sub>2</sub> onto Mo<sub>2</sub>CT<sub>x</sub>.

We also characterized Cu/Mo<sub>2</sub>CT<sub>x</sub>/SiO<sub>2-2h</sub> by high-resolution HAADF-STEM without exposing this material to air (Fig. 1d–f). Mo<sub>2</sub>CT<sub>x</sub> nanosheets are found to cover approximately one third of the silica surface. Stacking faults of the Mo<sub>2</sub>CT<sub>x</sub> lattice can be observed, indicated by the fast Fourier transform (FFT) pattern (Fig. 1d), which suggests the presence of Mo vacancies in Mo<sub>2</sub>CT<sub>x</sub> that may serve as interaction sites for Cu atoms<sup>34,38</sup>. Interestingly, while the SiO<sub>2</sub> surface that is not covered by MXene nanosheets in Cu/Mo<sub>2</sub>CT<sub>x</sub>/SiO<sub>2-2h</sub> contains Cu nanoparticles of ca. 3 nm in diameter, the Cu on the Mo<sub>2</sub>CT<sub>x</sub> nanosheets has a higher dispersion, including few-atoms-small clusters and single Cu atoms (circles, Fig. 1e). It is worth noting that the edges of the Mo<sub>2</sub>CT<sub>x</sub> nanosheets are decorated

with, most probably, Cu atoms, as indicated by arrows in Fig. 1f, which is reminiscent of the coordination of transition metals to the edges of MoS<sub>2</sub> layers in hydrotreating catalysts<sup>39</sup> or the decoration of graphene edges by Cu atoms<sup>40</sup>. This notable difference in the Cu speciation between the SiO<sub>2</sub> surface and Mo<sub>2</sub>CT<sub>x</sub> nanosheets is consistent with the high dispersion of Cu on β-Mo<sub>2</sub>C that has been reported previously<sup>23</sup>. No diffraction peaks due to Cu or Mo<sub>2</sub>CT<sub>x</sub> are observed in the X-ray powder diffraction (XRD) pattern of Cu/Mo<sub>2</sub>CT<sub>x</sub>/SiO<sub>2-2h</sub> that shows mainly the diffuse scattering of the amorphous SiO<sub>2</sub> support (Supplementary Figure 5).

The amounts of surface Cu<sup>0</sup> sites determined by N<sub>2</sub>O titration<sup>41</sup> (denoted Cu<sup>0</sup>(surf)) are 184.1, 78.4, and 59.4 μmol g<sub>cat</sub><sup>-1</sup> in Cu/SiO<sub>2-2h</sub>, Cu/Mo<sub>2</sub>CT<sub>x</sub>/SiO<sub>2-2h</sub>, and Cu/Mo<sub>2</sub>CT<sub>x</sub>/SiO<sub>2-6h</sub>, respectively (Supplementary Table 1). The surface Cu<sup>0</sup> sites account for 39% of the total Cu (measured by ICP analysis) in Cu/SiO<sub>2-2h</sub> (Supplementary Table 1). In contrast, surface Cu<sup>0</sup> sites contribute to only 21 and 16% of the total Cu sites in Cu/Mo<sub>2</sub>CT<sub>x</sub>/SiO<sub>2-2h</sub> and Cu/Mo<sub>2</sub>CT<sub>x</sub>/SiO<sub>2-6h</sub>, although similar particle size distributions are observed by TEM for Cu on the silica surface in Cu/SiO<sub>2-2h</sub> and Cu/Mo<sub>2</sub>CT<sub>x</sub>/SiO<sub>2</sub>. Note also that, as was discussed above, the Cu dispersion on the Mo<sub>2</sub>CT<sub>x</sub> nanosheets is notably higher than on the silica surface (small clusters and isolated atoms, Fig. 1d–f). Therefore, the lower fraction of surface Cu<sup>0</sup> sites determined in Cu/Mo<sub>2</sub>CT<sub>x</sub>/SiO<sub>2</sub> compared to Cu/SiO<sub>2-2h</sub> suggest the presence of surface Cu<sup>+</sup> sites in these materials that do not react with N<sub>2</sub>O (vide infra).

### **Catalytic performance of Cu/Mo<sub>2</sub>CT<sub>x</sub>/SiO<sub>2</sub>**

We then evaluated Cu/Mo<sub>2</sub>CT<sub>x</sub>/SiO<sub>2-6h</sub>, Cu/Mo<sub>2</sub>CT<sub>x</sub>/SiO<sub>2-2h</sub> and Cu/SiO<sub>2-2h</sub> for the hydrogenation of CO<sub>2</sub> at 230 °C and 25 bar (H<sub>2</sub>/CO<sub>2</sub>/N<sub>2</sub> = 3/1/1). Compared to the reference catalyst Cu/SiO<sub>2-2h</sub> (also prepared by SOMC), the intrinsic methanol formation rate of Cu/Mo<sub>2</sub>CT<sub>x</sub>/SiO<sub>2-2h</sub> is over three times higher (1.51 vs. 0.41 g h<sup>-1</sup> g<sub>Cu</sub><sup>-1</sup>, Fig. 1g), while the methanol selectivity is moderately higher (54% and 45%, Fig. 1g). Note that Mo<sub>2</sub>CT<sub>x</sub>/SiO<sub>2-2h</sub>

(i.e. the respective material without Cu) exhibits only a low methanol space-time yield (STY) and 63% selectivity to CO via RWGS (Supplementary Figures 8 and 9). Using Cu/Mo<sub>2</sub>CT<sub>x</sub>/SiO<sub>2-6h</sub>, which was prepared by increasing the duration of the treatment under H<sub>2</sub> to 6 h, leads to a further increase in the intrinsic methanol formation rate by 65% (to 2.49 g h<sup>-1</sup> g<sub>Cu</sub><sup>-1</sup> in Cu/Mo<sub>2</sub>CT<sub>x</sub>/SiO<sub>2-6h</sub>) with a similar methanol selectivity of 52%. Contrary to the Cu/β-Mo<sub>2</sub>C catalyst, no competing methanation of CO<sub>2</sub> was detected with Cu/Mo<sub>2</sub>CT<sub>x</sub>/SiO<sub>2</sub> catalysts, which contributes to a higher methanol selectivity on Cu/Mo<sub>2</sub>CT<sub>x</sub>/SiO<sub>2</sub> catalysts relative to Cu/β-Mo<sub>2</sub>C<sup>24</sup>. In addition, the Cu/Mo<sub>2</sub>CT<sub>x</sub>/SiO<sub>2</sub> catalysts developed in this study were compared to the benchmark Cu-ZnO-Al<sub>2</sub>O<sub>3</sub> catalyst. We note that the amounts of active sites in Cu-ZnO-Al<sub>2</sub>O<sub>3</sub> and Cu/Mo<sub>2</sub>CT<sub>x</sub>/SiO<sub>2</sub> catalysts are unknown. Therefore, we compare the intrinsic methanol formation rates in these catalysts after their normalization per Cu weight content (Fig. 1g and Supplementary Figures 10–12). Cu/Mo<sub>2</sub>CT<sub>x</sub>/SiO<sub>2-6h</sub> exceeds the activity of the benchmark Cu-ZnO-Al<sub>2</sub>O<sub>3</sub> catalyst (with high Cu loading) by 3.6 times (see Fig. 1g, Supplementary Figures 10–15, and Supplementary Table 3 for details). We note that the conversion of CO<sub>2</sub> is lower in experiments using the Cu/Mo<sub>2</sub>CT<sub>x</sub>/SiO<sub>2</sub> catalysts relative to the industrial Cu-ZnO-Al<sub>2</sub>O<sub>3</sub> catalyst due to the higher loading of Cu in Cu-ZnO-Al<sub>2</sub>O<sub>3</sub> catalyst, i.e. ca. 2.4 vs. 60 wt% Cu, respectively). At the same CO<sub>2</sub> conversion of 1.0%, the methanol selectivity increases as follows: Cu/SiO<sub>2-2h</sub> < Cu/Mo<sub>2</sub>CT<sub>x</sub>/SiO<sub>2-2h</sub> < Cu/Mo<sub>2</sub>CT<sub>x</sub>/SiO<sub>2-6h</sub> (33, 42, and 47%, respectively, Fig. 1h). A comparison between the Cu/Mo<sub>2</sub>CT<sub>x</sub>/SiO<sub>2</sub> catalysts reduced at 350 or 500 °C for 6 h indicates that reduction at 500 °C provides a more active catalyst (Supplementary Figure 16). No further notable increase of the activity of Cu/Mo<sub>2</sub>CT<sub>x</sub>/SiO<sub>2</sub> is observed when extending the duration of the treatment under H<sub>2</sub> at 500 °C even further (i.e. > 6 h, Fig. 1i). A control experiment shows that when Cu/Mo<sub>2</sub>CT<sub>x</sub>/SiO<sub>2</sub> was pretreated in H<sub>2</sub> at 500 °C for 2 h first, followed by an additional 2 h pretreatment in N<sub>2</sub> at 500 °C, the activity did not increase, suggesting that H<sub>2</sub> is critical for



the activation of the catalyst. A similar influence of a longer H<sub>2</sub> pretreatment time on the activity of Cu/SiO<sub>2</sub> is not observed, indicating that the increase in activity was due to the interaction of Cu and Mo<sub>2</sub>CT<sub>x</sub>. These results imply that the Cu-Mo<sub>2</sub>CT<sub>x</sub> interaction (vide infra for the discussion of the nature of this interaction) and the high dispersion of Cu on Mo<sub>2</sub>CT<sub>x</sub> is critical to obtain an enhanced activity for CO<sub>2</sub> hydrogenation to methanol.

After more than 20 h of time on stream (TOS), the activity and selectivity of both Cu/Mo<sub>2</sub>CT<sub>x</sub>/SiO<sub>2</sub> catalysts remained unchanged, demonstrating a high stability of the material (Supplementary Figure 17). An experiment with more than 100 h TOS using Cu/Mo<sub>2</sub>CT<sub>x</sub>/SiO<sub>2-6h</sub> was also performed and showed a stable methanol space time yield throughout the entire experiment, i.e. indicating no deactivation with TOS (Supplementary Figure 18). According to HAADF-EDX mapping (Supplementary Figure 19), the MXene morphology is preserved after 24 h of TOS of CO<sub>2</sub> hydrogenation, and the Cu distribution in the used Cu/Mo<sub>2</sub>CT<sub>x</sub>/SiO<sub>2-2h</sub> catalyst is similar to that in the fresh material. No sintering of the Cu NPs on the SiO<sub>2</sub> surface ( $3.0 \pm 0.3$  nm) is observed (Supplementary Figure 3).

To understand how the Cu-Mo<sub>2</sub>CT<sub>x</sub> interface in the Cu/Mo<sub>2</sub>CT<sub>x</sub>/SiO<sub>2</sub> catalysts may influence the mechanistic pathways for CO<sub>2</sub> hydrogenation, we performed a contact time study by changing the flow rates of the reactants. While the intrinsic methanol formation rate is high for the Cu/Mo<sub>2</sub>CT<sub>x</sub>/SiO<sub>2</sub> catalysts, it decreases with increasing contact time and CO<sub>2</sub> conversion, i.e. for Cu/Mo<sub>2</sub>CT<sub>x</sub>/SiO<sub>2-6h</sub> from 2.1 to 1.2 g h<sup>-1</sup> g<sub>Cu</sub><sup>-1</sup> at 0.7% and 3.2% CO<sub>2</sub> conversion, respectively (Supplementary Figure 6). However, the rates of Cu/Mo<sub>2</sub>CT<sub>x</sub>/SiO<sub>2-6h</sub> are still 2.5 times higher than for the Cu/SiO<sub>2-2h</sub> reference catalyst at the same contact time, which can be attributed to highly dispersed Cu on Mo<sub>2</sub>CT<sub>x</sub> nanosheets in Cu/Mo<sub>2</sub>CT<sub>x</sub>/SiO<sub>2</sub>. A similar decrease in the methanol formation rate has been observed for other Cu-based catalysts and is explained by the inhibition of methanol formation pathways by reaction

products, i.e. water and/or methanol<sup>12,13</sup>. In contrast, the CO formation rate increases slightly at long contact times for the Cu/Mo<sub>2</sub>CT<sub>x</sub>/SiO<sub>2</sub> catalysts. This result indicates that on Cu/Mo<sub>2</sub>CT<sub>x</sub>/SiO<sub>2</sub>, the mechanisms leading to the products methanol and CO are different. In addition, the methanol formation rate does not change significantly with contact time for Cu/SiO<sub>2-2h</sub>, implying different active sites in these two catalysts.

### **Rationale for higher activity of Cu/Mo<sub>2</sub>CT<sub>x</sub>/SiO<sub>2-6h</sub>**

One possible reason for the increasing activity of Cu/Mo<sub>2</sub>CT<sub>x</sub>/SiO<sub>2</sub> catalysts with increasing duration of the hydrogen treatment can be a different coverage of the Mo surface by T<sub>x</sub> groups in the supported MXene nanosheets. We have shown previously that the oxygen surface coverage in 2D-Mo<sub>2</sub>CO<sub>x</sub>/SiO<sub>2</sub> influences drastically the catalytic properties of this catalyst in the dry reforming of methane<sup>30</sup>. Therefore, we turned to X-ray photoelectron spectroscopy (XPS) analysis and fitted Mo<sup>5+</sup>, Mo<sup>4+</sup>, and carbidic Mo states in the Mo 3d XPS spectra of the MXene-derived materials (Supplementary Figure 20 and Supplementary Table 4). Mo is found mainly in the Mo<sup>5+</sup> and Mo<sup>4+</sup> states (69 and 22% fitted fractions, respectively) in CuMes/Mo<sub>2</sub>CT<sub>x</sub>/SiO<sub>2</sub> (i.e. before the H<sub>2</sub> treatment), due to the presence of abundant –O–, –OH, and –F groups oxidizing the surface after the synthesis of Mo<sub>2</sub>CT<sub>x</sub> (etching of the precursor phase Mo<sub>2</sub>Ga<sub>2</sub>C with 48% HF at 55 °C)<sup>42</sup>. XPS data shows no F 1s signal (688 eV) in Cu/Mo<sub>2</sub>CT<sub>x</sub>/SiO<sub>2-2h</sub>, in contrast to CuMes/Mo<sub>2</sub>CT<sub>x</sub>/SiO<sub>2</sub> (Supplementary Figure 21). After the H<sub>2</sub> treatment at 500 °C (2 h), the fraction of carbidic Mo increases from 9 to 54% at the expense of Mo<sup>5+</sup> and Mo<sup>4+</sup> states that decrease to 41% and 5%, respectively. A further reduction of Mo is observed in Cu/Mo<sub>2</sub>CT<sub>x</sub>/SiO<sub>2-6h</sub> (H<sub>2</sub> treatment at 500 °C for 6 h) as the fraction of Mo<sup>5+</sup> in this material is 30%, while the Mo<sup>4+</sup> state and carbidic Mo constitute 16% and 54%, respectively. After 24 h of TOS, the distribution of Mo states does not change notably, implying that surface Mo is not oxidized or reduced under CO<sub>2</sub> hydrogenation conditions (Supplementary Figure 22 and Supplementary Table 4).

Likewise, a continuous shift of Mo K-edge to lower energies was observed in an in situ X-ray absorption near edge structure (XANES) experiment, in which Cu/Mo<sub>2</sub>CT<sub>x</sub>/SiO<sub>2-0.5h</sub>, exposed to ambient air during the transfer of the material to a capillary cell reactor, was heated from room temperature to 500 °C in a flow of H<sub>2</sub> (Supplementary Figure 23). During this temperature-programmed reduction (TPR) experiment, the average oxidation state of Mo, estimated from the Mo K-edge position of XANES spectra<sup>43</sup>, reduced from ca. +4.4 in Cu/Mo<sub>2</sub>CT<sub>x</sub>/SiO<sub>2-0.5h</sub> at room temperature (RT) in air, to ca. +0.9 after 6 h under H<sub>2</sub> flow (500 °C), i.e. close to the Mo oxidation state in β-Mo<sub>2</sub>C<sup>28</sup>. The ex situ Mo K-edge XANES spectra of CuMes/Mo<sub>2</sub>CT<sub>x</sub>/SiO<sub>2</sub> and Cu/Mo<sub>2</sub>CT<sub>x</sub>/SiO<sub>2-6h</sub> (reduced in a laboratory reactor and handled without exposure to air) showed that the average oxidation state of Mo changed from ca. +4.8 to +0.9, corresponding to a shift in the Mo K-edge energy from 20013.5 to 20002.5 eV (Supplementary Figure 24). Overall, XPS and XANES results indicate a reduction of Mo sites in Mo<sub>2</sub>CT<sub>x</sub> in both H<sub>2</sub> treated materials, owing to a de-functionalization of the T<sub>x</sub> groups at the MXene surface.

To investigate if the Mo state changes during the CO<sub>2</sub> hydrogenation reaction, we performed an operando XANES investigation at the Mo K-edge at 230 °C and under 10 bar of reactants, with the products measured simultaneously by a gas chromatography (GC). In agreement with the XPS results, operando XANES data shows no notable change in the oxidation state of Mo and its local environment with TOS (2 h), which is corroborated by a stable methanol STY and selectivity (Supplementary Figure 25). Results of the operando XANES experiment are consistent with laboratory catalytic tests and the observed stability within 24 h of TOS (Supplementary Figure 17).

The presence of Cu<sup>+</sup> is identified in CuMes/Mo<sub>2</sub>CT<sub>x</sub>/SiO<sub>2</sub> owing to a low-intensity satellite feature at 942 eV in the Cu 2p XPS region (Supplementary Figure 26). While the H<sub>2</sub>

treatment leads to the disappearance of this subtle feature, in line with the reduction of  $\text{Cu}^+$  in the grafted species to metallic copper, the Cu  $L_3VV$  Auger region is more sensitive to  $\text{Cu}^+$  sites identified at 915.2 eV (Fig. 2a and Supplementary Table 5)<sup>44</sup>. Only a small fraction of less than 10% of  $\text{Cu}^+$  sites is detected in  $\text{Cu}/\text{SiO}_2\text{-2h}$ , which is likely owing to the interfacial  $\text{Cu-O-Si}\equiv$  sites, given the absence of C-H bands from the CuMes precursor in the IR spectrum of  $\text{Cu}/\text{SiO}_2\text{-2h}$  (Fig. 1b). Instead, Cu is mostly present in  $\text{Cu}/\text{SiO}_2\text{-2h}$  as a  $\text{Cu}^0$  phase identified by a peak centered at 918.4 eV. On the contrary, increasing amounts of  $\text{Cu}^+$  are observed in  $\text{Cu}/\text{Mo}_2\text{CT}_x/\text{SiO}_2\text{-2h}$  and  $\text{Cu}/\text{Mo}_2\text{CT}_x/\text{SiO}_2\text{-6h}$  (ca. 21 and 31%, respectively). Interestingly, the  $\text{Cu}^+$  fraction grows with increasing reduction time (from 2 h to 6 h) and this occurs simultaneously with the decrease of  $\text{Mo}^{5+}$  states and increase of  $\text{Mo}^{4+}$  states. This reduction of Mo can be due to the deoxygenation of the surface oxygen in  $\text{Mo}_2\text{CO}_x$  oxycarbide 2D nanosheets by  $\text{H}_2$ . However, because the increase in the fraction of  $\text{Cu}^+$  sites (i.e., oxidation of metallic copper) occurs simultaneously with the reduction of molybdenum, it is likely that surface  $\mu$ -oxo sites ( $\text{Mo-O-Mo}$ ) of  $\text{Mo}_2\text{CO}_x$  interact with  $\text{Cu}^0$  by forming  $\text{Mo-O-Cu}^+$  linkages and thereby reduce Mo (Fig. 1a). The increase in the fraction of  $\text{Cu}^+$  sites correlates with both the increasing catalytic activity and selectivity of the catalysts for  $\text{CO}_2$  hydrogenation to methanol (i.e.  $\text{Cu}/\text{SiO}_2\text{-2h} < \text{Cu}/\text{Mo}_2\text{CT}_x/\text{SiO}_2\text{-2h} < \text{Cu}/\text{Mo}_2\text{CT}_x/\text{SiO}_2\text{-6h}$ ). After 24 h of TOS, the amount of  $\text{Cu}^+$  does not change significantly, indicating the stability of the Cu sites under reactive conditions (Supplementary Figures 27 and 28, Supplementary Table 5).

In addition to Mo K-edge XANES, Cu K-edge X-ray absorption spectroscopy (XAS) data were acquired during the in situ  $\text{H}_2$  TPR capillary experiment described above, and showed a decrease of the edge position and white line intensity with heating; according to the Cu K-edge XAS data the formation of metallic Cu occurs at ca. 230 °C (Supplementary Figure 29). There is no significant change of the Cu state after the reduction of  $\text{Cu}/\text{Mo}_2\text{CT}_x/\text{SiO}_2\text{-0.5h}$

(exposed to air and then treated under H<sub>2</sub> from RT to 500 °C) for 5.5 h at 500 °C (Supplementary Figure 30). Concerning the Cu K-edge XAS experiments, it is worth noting that at this stage we cannot exclude the reduction of Cu<sup>+</sup> to metallic copper due to beam damage<sup>45</sup>. Based on the fittings of the extended X-ray absorption fine structure (EXAFS) functions of Cu/Mo<sub>2</sub>CT<sub>x</sub>/SiO<sub>2-6h</sub> and Cu/SiO<sub>2-2h</sub> (Supplementary Figures 31–33), a shorter interatomic Cu–Cu distance is observed in Cu/Mo<sub>2</sub>CT<sub>x</sub>/SiO<sub>2-6h</sub> (2.534(5) Å) compared with Cu/SiO<sub>2-2h</sub> (2.519(4) Å) likely due to the small clusters of Cu on Mo<sub>2</sub>CT<sub>x</sub>, and thus higher dispersion of the Cu phase or due to different particle shapes<sup>46</sup> (Supplementary Table 6). Importantly, we observe no evidence of alloying of Cu with Mo, in contrast to what has been reported for the reduction of Pt on Ti- or Nb-based MXene<sup>31,32</sup>. During the CO<sub>2</sub> hydrogenation reaction, the operando XAS data collected at the Cu K-edge shows no notable changes with TOS, indicating the stability of the Cu phase(s) under reaction conditions (Supplementary Figure 25 and Supplementary Table 6).

Next, to investigate the redox properties of Cu in the prepared materials, we compared the H<sub>2</sub> TPR behaviour of the materials after their oxidation by 5% O<sub>2</sub> at room temperature. The total amount of H<sub>2</sub> consumed to reduce the oxidized Cu/SiO<sub>2-2h</sub> is consistent with the expected amount of H<sub>2</sub> based on the Cu loading determined by ICP (96%, Supplementary Table 1), indicating that most of the Cu sites in Cu/SiO<sub>2-2h</sub> were oxidized to CuO and then reduced to metallic Cu with a maximum in the H<sub>2</sub> TPR profile at 168 °C (Fig. 2b). However, for Cu/Mo<sub>2</sub>CT<sub>x</sub>/SiO<sub>2-2h</sub> oxidized in the same conditions, the H<sub>2</sub> consumption constitutes only 68% of the total Cu measured by ICP while the TPR profile shows a broader, unsymmetrical peak compared to that of oxidized Cu/SiO<sub>2-2h</sub>, centered at a ca. 15 °C higher reduction temperature (Fig. 2b). This phenomenon is more pronounced for Cu/Mo<sub>2</sub>CT<sub>x</sub>/SiO<sub>2-6h</sub>, which shows a maximum at a reduction temperature of 201 °C. In contrast, the reference material Mo<sub>2</sub>CT<sub>x</sub>/SiO<sub>2-2h</sub> with the same Mo loading does not show notable H<sub>2</sub> consumption peaks in

the TPR after it has been oxidized. This data can be rationalized taking into account the increasing amount of  $\text{Cu}^+$  sites in  $\text{Cu}/\text{Mo}_2\text{CT}_x/\text{SiO}_2$  that has been exposed to a longer reductive pretreatment. It is likely that such  $\text{Cu}^+$  sites are not oxidized by 5%  $\text{O}_2$  at room temperature, which then accounts for the decreased consumption of  $\text{H}_2$  in the TPR experiment. That being said, two other effects might contribute to the observed TPR results. First, it has been reported that Cu on  $\beta\text{-Mo}_2\text{C}$  exhibits strong electronic metal-support interaction that leads to a partial charge transfer from Cu atoms to  $\beta\text{-Mo}_2\text{C}$ , which aids the high dispersion of copper<sup>23</sup>. In addition, Cu might fill positions of Mo vacancies in the structure of  $\text{Mo}_2\text{CT}_x$ , similarly to what was reported for single Pt atoms confined in vacancies of  $\text{Ti}_3\text{C}_2\text{T}_x$ <sup>34</sup>. At this stage, it is not clear to what extent these two alternatives play a role in the oxidation-reduction behaviour of the  $\text{Cu}/\text{Mo}_2\text{CT}_x/\text{SiO}_2$  system.

Additional temperature-programmed desorption (TPD) of  $\text{H}_2$  experiments allowed us to verify the different nature of the Cu sites in the prepared catalysts. While only one  $\text{H}_2$  desorption peak is observed for  $\text{Cu}/\text{SiO}_2\text{-2h}$  at 20 °C, two peaks are observed for  $\text{Cu}/\text{Mo}_2\text{CT}_x/\text{SiO}_2\text{-2h}$  and  $\text{Cu}/\text{Mo}_2\text{CT}_x/\text{SiO}_2\text{-6h}$  at 20 and 40 °C (Fig. 2c). This suggests that the desorption peaks at 20 and 40 °C are, respectively, due to Cu on the  $\text{SiO}_2$  surface and Cu sites on  $\text{Mo}_2\text{CT}_x$ . Analysis of the relative peak areas indicates that the fraction of  $\text{Cu}/\text{Mo}_2\text{CT}_x$  sites increased from 44% in  $\text{Cu}/\text{Mo}_2\text{CT}_x/\text{SiO}_2\text{-2h}$  to 55% in  $\text{Cu}/\text{Mo}_2\text{CT}_x/\text{SiO}_2\text{-6h}$  (Supplementary Table 7). The  $\text{H}_2$  capacity of  $\text{Cu}/\text{SiO}_2$ ,  $\text{Cu}/\text{Mo}_2\text{CT}_x/\text{SiO}_2\text{-2h}$  and  $\text{Cu}/\text{Mo}_2\text{CT}_x/\text{SiO}_2\text{-6h}$ , calculated from  $\text{H}_2$ -TPD data, are 35.2, 18.1, and 9.5  $\mu\text{mol g}_{\text{cat}}^{-1}$ , respectively (Supplementary Table 1). We explain this trend by the increasing fraction of surface  $\text{Cu}^+$  sites with increasing duration of the reductive pretreatment, as was already discussed above.

Diffuse reflectance infrared Fourier transform spectroscopy (DRIFTS) using CO as the probe molecule was used to evaluate the electronic properties of the copper sites on the surfaces of

SiO<sub>2</sub> and Mo<sub>2</sub>CT<sub>x</sub>. Experiments were performed using a Praying Mantis reaction cell with in situ reduced materials (H<sub>2</sub>, 500 °C) that were then exposed to 10% CO/N<sub>2</sub> for 10 min and flushed with N<sub>2</sub> for 60 min at room temperature. Under these conditions, CO desorbs from weakly bound CO–Cu<sup>0</sup> adducts<sup>37</sup>, while stronger bound CO–Cu<sup>+</sup> adducts remain present. Upon binding of CO, a main peak at 2124 cm<sup>-1</sup> and a shoulder at 2112 cm<sup>-1</sup> are observed for Cu/SiO<sub>2-2h</sub> (Fig. 2d), consistent with previous studies<sup>47</sup>. The intensity of the peaks of adsorbed CO on Cu/SiO<sub>2-2h</sub> decreases at 100 °C and the peaks eventually disappear at 200 °C in N<sub>2</sub> flow due to the desorption of CO. However, in both Cu/Mo<sub>2</sub>CT<sub>x</sub>/SiO<sub>2</sub> catalysts, there is an additional blue-shifted feature at 2134 cm<sup>-1</sup> and its intensity is higher for Cu/Mo<sub>2</sub>CT<sub>x</sub>/SiO<sub>2-6h</sub> than for Cu/Mo<sub>2</sub>CT<sub>x</sub>/SiO<sub>2-2h</sub>. The peak at 2134 cm<sup>-1</sup> is observed even at 200 °C, in contrast to the bands at 2124 and 2112 cm<sup>-1</sup> attributed to CO–Cu<sup>+</sup> adducts on Cu/SiO<sub>2-2h</sub>. Note that without Cu, Mo<sub>2</sub>CT<sub>x</sub>/SiO<sub>2-2h</sub> does not absorb CO at room temperature (Supplementary Figure 35). The CO adsorption peak at 2134 cm<sup>-1</sup> is ascribed therefore to the presence of Cu<sup>+</sup> sites on Mo<sub>2</sub>CT<sub>x</sub><sup>48,49</sup>. An alternative explanation that, however, appears less likely is that highly dispersed metallic Cu (vacancy-confined single Cu atoms in the lattice of Mo<sub>2</sub>CT<sub>x</sub> or small Cu clusters in the electronic interaction with the support) give more stable CO adducts. The higher stability of CO–Cu<sup>+</sup> adducts relative to CO–Cu<sup>0</sup> is due to the stronger σ-donation from the highest occupied molecular orbital (HOMO) of CO to the more Lewis acidic (relative to metallic Cu) Cu<sup>+</sup> sites<sup>44,50</sup>. Depletion of electron density from the slightly antibonding HOMO of CO leads to the observed blue shift and strengthens the CO–Cu<sup>+</sup> interaction, while the π-backbonding interaction may be only slightly reduced in CO–Cu<sup>+</sup> relative to that in CO–Cu<sup>0</sup> adducts<sup>44,51</sup>. It is likely that the enhanced activity of Cu/Mo<sub>2</sub>CT<sub>x</sub>/SiO<sub>2-6h</sub> in CO<sub>2</sub> hydrogenation is due to the Cu<sup>0</sup>/Cu<sup>+</sup>/Mo<sub>2</sub>CT<sub>x</sub> interface, which is reminiscent of the Cu<sup>0</sup>/Cu<sup>+</sup>/CeO<sub>2-x</sub> interface reported recently<sup>44</sup>. Overall, the CO DRIFTS results (after the desorption of CO from Cu<sup>0</sup> sites in N<sub>2</sub> flow) are consistent with the presence

of  $\text{Cu}^+$  sites that bind CO strongly (band at  $2134\text{ cm}^{-1}$ ) in  $\text{Cu}/\text{Mo}_2\text{CT}_x/\text{SiO}_2$  material, assigned to  $\text{Cu}^+$  on  $\text{Mo}_2\text{CT}_x$  nanosheets. The peak positions of CO adsorbed on  $\text{Cu}^+$  sites are unchanged in  $\text{Cu}/\text{Mo}_2\text{CT}_x/\text{SiO}_2\text{-2h}$  and  $\text{Cu}/\text{Mo}_2\text{CT}_x/\text{SiO}_2\text{-6h}$ . Overall, Cu XPS (Auger peaks),  $\text{H}_2$  TPR,  $\text{H}_2$  TPD, and CO DRIFTS data suggests that a longer thermal treatment in  $\text{H}_2$  at  $500\text{ }^\circ\text{C}$  (6 h vs. 2 h) unexpectedly results in a higher fraction of  $\text{Cu}^+$  sites on the  $\text{Mo}_2\text{CT}_x$  phase, which proceeds in parallel with the reduction of Mo sites in  $\text{Mo}_2\text{CT}_x$ . Thus, while the atomically thin  $\text{Mo}_2\text{CT}_x$  nanosheet support is reducible<sup>30</sup>, it lacks the typical SMSI overcoating effect of typical metal oxide supports (bulk or nanoparticles, e.g.  $\text{TiO}_2$ ,  $\text{CeO}_2$ , ...). Therefore, as the  $\text{Cu}^0/\text{Cu}^+$  interface appears to be related on  $\text{CeO}_2$  and on  $\text{Mo}_2\text{CT}_x$ , it is the absence of an encapsulation of the active phase by the reduced support on rigid, thermally stable  $\text{Mo}_2\text{CT}_x$  nanosheets<sup>30</sup>, which do not change their 2D morphology with TOS (vide infra), that is likely responsible for the improved catalytic performance of  $\text{Cu}/\text{Mo}_2\text{CT}_x/\text{SiO}_2$ .

### **Nature of Cu sites from $\text{Cu}/\text{Mo}_2\text{CO}_x$ models**

Periodic density functional theory (DFT) calculations using the BEEF-vdW density functional<sup>52</sup> were carried out to improve our understanding of the nature of Cu sites in  $\text{Cu}/\text{Mo}_2\text{CT}_x/\text{SiO}_2\text{-2h}$  and  $\text{Cu}/\text{Mo}_2\text{CT}_x/\text{SiO}_2\text{-6h}$  catalysts and to refine the possible interaction between Cu and  $\text{Mo}_2\text{CO}_x$  nanosheets. A  $3\times 3$ -unit cell derived from a  $\text{Mo}_2\text{C}$  (001) surface slab containing two Mo layers, one at the top and one at the bottom of the slab, and one middle carbon layer, in agreement with the stoichiometry of the material, was used to model the  $\text{Mo}_2\text{CO}_x$  surface. A further description of the methodology and details of the  $\text{Mo}_2\text{C}$  model<sup>30</sup> as well as the reference Cu (111) and  $\text{Cu}_2\text{O}$  (111) surfaces can be found in Supplementary Figures 36 and 37. First, we supported one and four Cu atoms on the  $3\times 3$  2D- $\text{Mo}_2\text{C}$  surface to generate the respective  $\text{Cu}/2\text{D-Mo}_2\text{C}$  (Model 1) and  $\text{Cu}_4/2\text{D-Mo}_2\text{C}$  (Model 1b) surface structures. In addition, we considered the following oxygen coverages for one supported Cu atom:  $2/9$ ,  $5/9$ ,



6/9 and 7/9 of a full oxygen monolayer (ML), denoted Model 2, 3, 4 and 5, respectively. These different oxygen coverages model various oxidation states of the  $\text{Mo}_2\text{CO}_x$  nanosheets of the experimental system, as was determined by the XANES and XPS analyses of the  $\text{Cu}/\text{Mo}_2\text{CT}_x/\text{SiO}_2\text{-2h}$  and  $\text{Cu}/\text{Mo}_2\text{CT}_x/\text{SiO}_2\text{-6h}$  catalysts discussed above.

First, we compared energies of hydrogen adsorption on the Cu (111) slab,  $\text{Cu}/2\text{D-Mo}_2\text{C}$ ,  $\text{Cu}_4/2\text{D-Mo}_2\text{C}$  and  $\text{Cu}/2\text{D-Mo}_2\text{C-0.67 O ML}$  (i.e. Model 4) by evaluating the dissociative adsorption of  $\text{H}_2$  forming atomic hydrogen species ( $\text{H}^*$ ). On Cu (111),  $\text{H}^*$  adsorbs on the hcp hollow site (Supplementary Figure 38), while on  $\text{Cu}/2\text{D-Mo}_2\text{C}$ ,  $\text{Cu}_4/2\text{D-Mo}_2\text{C}$ , and  $\text{Cu}/2\text{D-Mo}_2\text{C-0.67 O ML}$  (Models 1, 1b, and 4),  $\text{H}^*$  adsorbs on the  $\text{Cu}/2\text{D-Mo}_2\text{C}$  interface with the respective electronic binding energies of  $-0.3$ ,  $-34$ ,  $-28$ , and  $-27 \text{ kJ mol}^{-1}$  with respect to the gas-phase  $\text{H}_2$  molecule, i.e. a stronger  $\text{H}^*$  adsorption is observed on all evaluated  $\text{Cu}/2\text{D-Mo}_2\text{C}$  interfaces in comparison to the Cu (111) slab (Fig. 2e–g). These results show that the interface in  $\text{Cu}/2\text{D-Mo}_2\text{C}$ ,  $\text{Cu}_4/2\text{D-Mo}_2\text{C}$  or  $\text{Cu}/\text{Mo}_2\text{CO}_x$  surfaces can be responsible for the stronger hydrogen adsorption, in agreement with the  $\text{H}_2$  TPD results (Fig. 2c) that revealed a higher temperature for  $\text{H}_2$  desorption for the  $\text{Cu}/\text{Mo}_2\text{CT}_x$  catalysts relative to the  $\text{Cu}/\text{SiO}_2$  reference catalyst (represented by the Cu (111) slab model in our DFT calculations). Yet, Model 4 represents our experimental systems better than Model 1, because Mo is oxidized in the  $\text{Cu}/\text{Mo}_2\text{CT}_x/\text{SiO}_2$  catalysts according to XANES and XPS results described above.

Next, we found that CO adsorbs preferentially atop of Cu in Models 1–5 featuring binding energies of  $-62$ ,  $-77$ ,  $-70$ ,  $-89$ , and  $-83 \text{ kJ mol}^{-1}$  for Models 1 to 5, respectively (Fig. 2h and i). According to the Bader charge analysis, Cu atoms with an adsorbed CO molecule in Models 4 and 5 have oxidation states of  $+0.6$  and  $+0.5$ , i.e. in these models Cu sites have the most significant  $\text{Cu}^{\delta+}$  character (Supplementary Figure 39), which correlates also with a higher CO binding energy and a stronger blue shift of vibrational frequency of CO with respect to

Cu/2D-Mo<sub>2</sub>C (Supplementary Table 9). The Cu<sup>δ+</sup> character becomes more notable upon CO adsorption (Supplementary Figure 39). We calculated the stretching frequency of CO on Cu (111) and Cu<sub>2</sub>O (111) reference surfaces and found that CO on the Cu (111) surface is red-shifted (2020 cm<sup>-1</sup>) and CO on the Cu<sub>2</sub>O (111) surface is blue-shifted (2093 cm<sup>-1</sup>, Supplementary Table 9). The latter frequency is comparable to the frequency of adsorbed CO in Models 4 and 5. This is consistent with the high Cu<sup>δ+</sup> character found using the Bader charge analysis for Cu sites in Models 4 and 5.

The calculated shift of the CO stretching frequency with respect to gas-phase CO is -38 cm<sup>-1</sup> for Model 4 and -30 cm<sup>-1</sup> for Model 5 (BEEF-vdW functional). When evaluated using the PBE0 functional, the calculated shift for Model 4 is -18 cm<sup>-1</sup>, which is close to the experimental shift of -9 cm<sup>-1</sup> (Supplementary Table 10). Overall, we conclude that Cu sites in Models 4 and 5 have a significant Cu<sup>δ+</sup> character, consistent with experimental results.

### **Characterization of reaction intermediates**

Two mechanistic pathways for CO<sub>2</sub> hydrogenation to methanol were proposed, *viz.* involving CO or formate as intermediates<sup>17,53</sup>. Our contact time experiments have identified CO and methanol as the primary products of CO<sub>2</sub> hydrogenation (Supplementary Figures 6 and 7, Supplementary Table 2); therefore intermediacy of CO in the formation of methanol is unlikely<sup>13</sup>. To explore the surface intermediates of CO<sub>2</sub> hydrogenation over the Cu/Mo<sub>2</sub>CT<sub>x</sub>/SiO<sub>2</sub> catalysts, we relied on an operando DRIFTS study with the simultaneous quantification of products by gas chromatography. At 230 °C and 25 bar (H<sub>2</sub>/CO<sub>2</sub>/N<sub>2</sub> = 3/1/1), formate (2936, 2857, and 2698 cm<sup>-1</sup>) and methoxy peaks (2996 and 2959 cm<sup>-1</sup>)<sup>13,54</sup> are identified on Cu/Mo<sub>2</sub>CT<sub>x</sub>/SiO<sub>2-2h</sub>, while carbonate or bicarbonate peaks are not observed (Fig. 3a and Supplementary Figure 40). The intensity of the bands owing to surface formate groups and the STY of methanol reaches a steady state after ca. 60 min of TOS, whereas the

intensity of peaks due to surface methoxy groups continues to increase for a substantially longer time, ca. 15 h. The amplitude of the bands due to surface formate and methoxy grows faster for Cu/Mo<sub>2</sub>CT<sub>x</sub>/SiO<sub>2-2h</sub> than for Cu/SiO<sub>2-2h</sub>, which correlates with a higher STY of methanol, as quantified by GC (Fig. 3b).

Note that the formate peaks are more intense on Cu/Mo<sub>2</sub>CT<sub>x</sub>/SiO<sub>2-2h</sub> than on Cu/SiO<sub>2-2h</sub> at lower pressures ( $\leq 20$  bar), including under atmospheric pressure (Supplementary Figure 41). The trend for the formation of a carbonyl band at 2077 cm<sup>-1</sup> (i.e. intermediate for CO) at different pressures is the opposite to that of formate, indicating the selective formation of methanol on the Cu/Mo<sub>2</sub>CT<sub>x</sub>/SiO<sub>2</sub> catalyst compared to Cu/SiO<sub>2</sub> (Supplementary Figure 41). To verify that the formate species are intermediates on the methanol synthesis pathway, Cu/Mo<sub>2</sub>CT<sub>x</sub>/SiO<sub>2-2h</sub> was exposed to a H<sub>2</sub>/CO<sub>2</sub>/N<sub>2</sub> (3/1/1) feed for 10 min at atmospheric pressure and then the CO<sub>2</sub> flow was discontinued. The surface formate bands decreased gradually while methanol was detected by GC (Supplementary Figure 42), implying that formate species could be hydrogenated by H<sub>2</sub> on Cu/Mo<sub>2</sub>CT<sub>x</sub>/SiO<sub>2-2h</sub> to methanol.

To further explore the nature of the reaction intermediates, we used solid-state <sup>13</sup>C NMR spectroscopy. This method provides primarily information on adsorbed intermediates on the support since intermediates on metallic copper can suffer from signal broadening and Knight shifts<sup>13</sup>. Cu/Mo<sub>2</sub>CT<sub>x</sub>/SiO<sub>2-2h</sub> was kept under 5 bar of <sup>1</sup>H<sub>2</sub>/<sup>13</sup>CO<sub>2</sub> (3/1) at 230 °C for 12 h followed by outgassing at room temperature and ssNMR analysis. The observed <sup>13</sup>C NMR chemical shift at 172 ppm is consistent with the presence of formate species (Fig. 3c), which is however not observed in <sup>1</sup>H NMR, probably due to a too weak or broad signal (Supplementary Figure 43). The formate peak is more deshielded on Cu/Mo<sub>2</sub>CT<sub>x</sub>/SiO<sub>2-2h</sub> (172 ppm) than on Cu/SiO<sub>2</sub> (168 ppm)<sup>13</sup>. Species with the <sup>13</sup>C chemical shift at 49 ppm and <sup>1</sup>H NMR chemical shift at 3.9 ppm are ascribed to surface -OCH<sub>3</sub> species (possibly, Cu-

OCH<sub>3</sub>). Note that these signals have not been observed on Cu/SiO<sub>2</sub> in the absence of Mo<sub>2</sub>CT<sub>x</sub><sup>13</sup> after reaction under 5 bar of <sup>1</sup>H<sub>2</sub>/<sup>13</sup>CO<sub>2</sub> (3/1), yet operando DRIFTS at 25 bar reveals methoxy bands on Cu/SiO<sub>2</sub> (Fig. 3b). No intermediates are observed on Mo<sub>2</sub>CT<sub>x</sub>/SiO<sub>2</sub>. Therefore, neither Cu NPs alone nor Mo<sub>2</sub>CT<sub>x</sub> alone can generate methoxy species from formate species under the conditions used for the <sup>13</sup>C NMR experiments (i.e. 230 °C and 5 bar) and it is the Cu dispersed on Mo<sub>2</sub>CT<sub>x</sub> nanosheets that yields the surface methoxy species. Furthermore, also formate species are not observed on Mo<sub>2</sub>CT<sub>x</sub>/SiO<sub>2</sub> (Fig. 3c).

### **DFT-computed reaction pathways over single atom Cu/Mo<sub>2</sub>CO<sub>x</sub>**

We performed DFT calculations using the BEEF-vdW functional<sup>52</sup> to obtain atomic-level insight into the pathway of CO<sub>2</sub> hydrogenation to methanol or CO on the Cu/2D-Mo<sub>2</sub>C-0.67 O ML surface (this model has been described above in Fig. 1g). This particular structure was selected as a realistic model for the DFT calculations and used to evaluate the respective energy profiles to form methanol or CO (Fig. 4). In what follows, we describe the most probable reaction pathways and aim to rationalize the experimental observations.

As oxygen covers only partially the 2D-Mo<sub>2</sub>C surface in our model, reactive Mo sites with a proximal Cu atom are accessible. The interaction of CO<sub>2</sub> and H<sub>2</sub> on the model surface is exoenergetic by merely 14 kJ mol<sup>-1</sup>, suggesting that both species are physisorbed, as also inferred from the very minor changes of the geometries of CO<sub>2</sub> and H<sub>2</sub> upon their interaction with the surface. These two physisorbed molecules then form formate (HCOO\*) and adsorbed H\*. This step proceeds via a transition state TS1, associated with an energy barrier of 103 kJ mol<sup>-1</sup>, which we interpret as the CO<sub>2</sub>-assisted heterolytic cleavage of H<sub>2</sub>. In TS1, CO<sub>2</sub> is significantly bent (∠O-C-O is ca. 125°) with one O pointing to Mo. The H<sub>2</sub> molecule is cleaved in TS1 heterolytically, i.e. forming simultaneously new C-H and Cu-H bonds. Since

both CO<sub>2</sub> and H<sub>2</sub> do not chemisorb on 2D-Mo<sub>2</sub>C-0.67 O ML for this step, it can be classified as Eley-Rideal type<sup>55</sup>. Note that HCOO\* species have been detected by DRFITS and <sup>13</sup>C MAS NMR spectroscopies (Fig. 3). The resulting formate intermediate (**2**, Fig. 4) is η<sup>2</sup>-coordinated at the Cu/2D-Mo<sub>2</sub>C-0.67 O ML interface such that one O of the formate is coordinated to Cu and the second O is coordinated to Mo. The H\* atom is also adsorbed at the Cu/2D-Mo<sub>2</sub>C-0.67 O ML interface. HCOO\* species can re-orient to coordinate both of its oxygen atoms to surface Mo in a low energy process via TS2 (52 kJ mol<sup>-1</sup>), likely due to the higher oxophilicity of Mo compared to Cu. This migration of the HCOO\* species on the 2D-Mo<sub>2</sub>C-0.67 O ML surface allows to stabilize the dioxymethylene species (H<sub>2</sub>COO\*, **5**, Fig. 4), as discussed below.

Previous DFT pathways of the hydrogenation of CO<sub>2</sub> to methanol on Cu or Cu-alloy surfaces proposed that the formation of H<sub>2</sub>COOH\* from HCOO\* species proceeds through formic acid (HCOOH\*)<sup>3</sup>. In contrast, on a Cu/2D-Mo<sub>2</sub>C-0.67 O ML surface, we have identified a pathway leading to the formation of H<sub>2</sub>COO\* from HCOO\* species, with similar energetics as in the literature<sup>3</sup>, which includes the H-transfer to the η<sup>2</sup>-coordinated formate via TS3. In this transition state, H<sub>2</sub> is cleaved heterolytically yielding H<sub>2</sub>COO\* and H\* species, that is forming C–H and Cu–H bonds in a pathway similar to TS1 discussed above. TS3 has the highest energy barrier (141 kJ mol<sup>-1</sup>) in the pathway of CO<sub>2</sub> hydrogenation to methanol, i.e. it is the rate-limiting transition state. The most favorable pathway to methanol from the H<sub>2</sub>COO\* and H\* species proceeds through formaldehyde (H<sub>2</sub>CO\*) and hydroxy (OH\*) species (**6**, Fig. 4). This pathway involves both the cleavage of the C–O bond of H<sub>2</sub>COO\* as well as the formation of OH\* species. It has been postulated that H<sub>2</sub> assistance is required for C–O bond cleavage on Cu/Mo<sub>2</sub>C surfaces<sup>24</sup>. Yet on the Cu/2D-Mo<sub>2</sub>C-0.67 O ML model surface, the formation of co-adsorbed H<sub>2</sub>CO\* and OH\* proceeds with a very low energy barrier of 16 kJ mol<sup>-1</sup> (TS4). In a subsequent TS5, with an energy barrier of 37 kJ mol<sup>-1</sup>, H-transfer from OH\* to H<sub>2</sub>CO\* leads

to methoxy ( $\text{CH}_3\text{O}^*$ ) and  $\text{O}^*$  (**7**). The intermediate structure **7** is located at  $-273 \text{ kJ mol}^{-1}$  and this high stability explains the observation of these species in FTIR and NMR experiments as described above. The regeneration of the  $\text{OH}^*$  species proceeds by the reaction of  $\text{H}^*$  with the  $\text{O}^*$  atom at the interface between Cu and 2D- $\text{Mo}_2\text{C}$ -0.67 O ML. This TS6 has an energy barrier of  $89 \text{ kJ mol}^{-1}$ . The last step generates methanol by proton transfer from the  $\text{OH}^*$  group to  $\text{OCH}_3^*$  via TS7, requiring  $57 \text{ kJ mol}^{-1}$ . The resulting  $\text{CH}_3\text{OH}^*$  species (**9**) is located at  $-243 \text{ kJ mol}^{-1}$  in the energy diagram. Methanol desorption requires  $87 \text{ kJ mol}^{-1}$ . Finally, the adsorbed  $\text{O}^*$  atom leads to the formation of water in a pathway that is shared with the RWGS reaction and explained in detail in the following section.

We note that starting from the  $\text{H}_2\text{COO}^*$  species, three alternative reaction pathways to form methanol are possible, which are however energetically less favorable than the pathway presented in Fig. 4. Two pathways involve the formation of  $\text{H}_2\text{COOH}^*$  as a reaction intermediate, while the third pathway features the direct C–O cleavage of  $\text{H}_2\text{COO}^*$ , forming formaldehyde ( $\text{H}_2\text{CO}^*$ ) and  $\text{O}^*$  in a single step. These pathways are discussed in Supplementary Figures 45–48.

We have also evaluated the energy profile of the competitive reverse water–gas shift reaction using the Cu/2D- $\text{Mo}_2\text{C}$ -0.67 O ML model (Fig. 4). The adsorption of  $\text{CO}_2$  (in the absence of  $\text{H}_2$ ) on the surface is exoenergetic by  $18 \text{ kJ mol}^{-1}$  (**11**) and leads to a bent  $\text{CO}_2$  (**12**,  $\angle\text{O–C–O}$  is ca.  $136^\circ$ ) at the interface of the Cu atom and the 2D- $\text{Mo}_2\text{C}$ -0.67 O ML surface via TS8 with an energy barrier of  $35 \text{ kJ mol}^{-1}$ . From intermediate **12**, C–O bond cleavage has a very low energy barrier of  $3 \text{ kJ mol}^{-1}$  (TS9). Thus,  $\text{CO}^*$  is readily formed by the direct activation of  $\text{CO}_2$  adsorbed at the Cu/2D- $\text{Mo}_2\text{C}$ -0.67 O ML interface yielding  $\text{CO}^*$  and  $\text{O}^*$  species.  $\text{CO}^*$  adsorbed on a Cu atom (**13**) is located at  $-109 \text{ kJ mol}^{-1}$  and desorption of CO from Cu in intermediate **13** requires  $80 \text{ kJ mol}^{-1}$ . This pathway to CO features relatively low activation

barriers compared to the methanol formation route, and is consistent with the experimentally observed formation of CO, along with methanol, in our catalytic tests. Following the desorption of CO, H<sub>2</sub> is adsorbed on the Cu atom, which is energetically favorable by 13 kJ mol<sup>-1</sup> (**15**). In this intermediate **15**, H<sub>2</sub> is coordinated to Cu in a η<sup>2</sup> mode with a H–H distance of 0.759 Å, and with respective Cu–H distances of 1.95 Å and 1.97 Å. In the next step, the heterolytic cleavage of H<sub>2</sub> yields simultaneously O–H and Cu–H bonds, forming intermediate **16**. This step is endoenergetic by 29 kJ mol<sup>-1</sup> with an energy barrier in TS10 of 73 kJ mol<sup>-1</sup>. Finally, H<sub>2</sub>O\* forms by the subsequent reaction of OH\* with H\* on the Cu/2D-Mo<sub>2</sub>C-0.67 O ML interface with an energy barrier of 100 kJ mol<sup>-1</sup> (in TS11), i.e. the rate-limiting step of the RWGS pathway. The resulted intermediate **17** is located 3 kJ mol<sup>-1</sup> higher than the initial reactants. The final step i.e. the desorption of water is endoenergetic and requires 65 kJ mol<sup>-1</sup>.

We have also evaluated an alternative RWGS mechanism involving the activation of H<sub>2</sub> to form 2H\* on the Cu/2D-Mo<sub>2</sub>C-0.67 O ML interface. This process, however, involves a high energy barrier of 144 kJ mol<sup>-1</sup> and is endoenergetic by 72 kJ mol<sup>-1</sup> (Supplementary Figure 49), which makes it energetically less favorable compared to the route described above. Overall, the presented RWGS mechanism (Fig. 4), including the heterolytic cleavage of H<sub>2</sub>, proceeds via the chemisorption of each reactive species and therefore follows a Langmuir-Hinshelwood type manifold<sup>56</sup> on our Cu/2D-Mo<sub>2</sub>C-0.67 O ML model, in contrast to the CO<sub>2</sub> hydrogenation pathway discussed above.

To summarize, DFT calculations highlight the likely intermediates and transition states and allow to propose a feasible energy profile for the pathways of CO<sub>2</sub> hydrogenation to methanol and CO on a Cu/2D-Mo<sub>2</sub>C-0.67 O ML model. The interface between a Cu atom and the 2D-Mo<sub>2</sub>C-0.67 O ML surface plays a crucial role in the CO<sub>2</sub> hydrogenation reactions. The Cu atom and the support both participate in the reaction mechanism by reducing the

energy barriers for successive heterolytic cleavages of H<sub>2</sub> that are required to form HCOO\*, H<sub>2</sub>COO\*, and H<sub>2</sub>COOH\* species, simultaneously with adsorbed H\*. The most energy-demanding step in the methanol production pathway is the formation of the H<sub>2</sub>COO\* species. The Cu/2D-Mo<sub>2</sub>C-0.67 O ML interface also provides a low energy route for CO<sub>2</sub> adsorption, followed by its direct cleavage into CO\* and O\*. Hence, on the Cu/2D-Mo<sub>2</sub>C-0.67 O ML model, both CH<sub>3</sub>OH and CO are easily obtained under CO<sub>2</sub> hydrogenation conditions, providing an explanation for the experimental observation of both products. Finally, the most strongly adsorbed reaction intermediates determined by our DFT calculations are HCOO\* and CH<sub>3</sub>O\*, that is the same intermediates that are observed in our operando DRIFTS and NMR experiments.

## CONCLUSIONS

In conclusion, our work demonstrates that highly dispersed Cu species, including single Cu atoms, can be enriched selectively on the Mo<sub>2</sub>CT<sub>x</sub> phase by migration from SiO<sub>2</sub> under reductive pretreatment. Consequently, the Cu/Mo<sub>2</sub>CT<sub>x</sub>/SiO<sub>2</sub> catalysts show two different Cu sites: Cu/Mo<sub>2</sub>CT<sub>x</sub> and Cu/SiO<sub>2</sub>. The Cu/Mo<sub>2</sub>CT<sub>x</sub> interface, with Lewis acidic Cu<sup>+</sup> sites, is responsible for the observed increased methanol formation rate and selectivity. These findings, complemented by DFT calculations, show the prospects of copper single atom catalysis for CO<sub>2</sub> hydrogenation exploiting metal-support interactions in general and Cu/MXenes interfaces in particular.

## Methods

### Catalyst preparation

SiO<sub>2</sub> (Aerosil 300) was compacted, sieved (180–300 μm), and calcined in static air (500 °C, 3 h). The calcined material had a surface area of 374 m<sup>2</sup> g<sup>-1</sup> and a pore volume of 2.0 mL g<sup>-1</sup>.



Mo<sub>2</sub>Ga<sub>2</sub>C was synthesized as reported previously<sup>28</sup> and treated in a 14 M HF solution at 55 °C for 7 days in a sealed Teflon-lined autoclave<sup>42</sup>. This gave a mixture of Mo<sub>2</sub>CT<sub>x</sub> and Mo<sub>2</sub>Ga<sub>2</sub>C phases that was washed and dried (Supplementary Figure 50). Ca. 2 g of this material was dispersed in 30 mL of 40% tetrabutylammonium hydroxide (TBAOH) and 10 mL of water and stirred at room temperature for 12 h. The solid was then separated via centrifugation (6000 rpm, 5 min) and washed with ethanol (2 × 40 mL) and water (3 × 40 mL), followed by sonication (40 min) and centrifugation (3500 rpm, 30 min). The supernatant containing colloidal solution of delaminated 2D-Mo<sub>2</sub>CT<sub>x</sub> nanosheets was collected (Supplementary Figure 1). Ca. 150 mL of this 2D-Mo<sub>2</sub>CT<sub>x</sub> solution was impregnated onto 5 g SiO<sub>2</sub> using incipient wetness impregnation (15 cycles of impregnation and drying under vacuum at 50 °C for 4 h). No Ga signal was observed in the X-ray photoelectron spectroscopy (XPS) of Mo<sub>2</sub>CT<sub>x</sub>/SiO<sub>2</sub> (Supplementary Figure 51), indicating that 2D-Mo<sub>2</sub>CT<sub>x</sub> was separated from the bulk Mo<sub>2</sub>Ga<sub>2</sub>C during centrifugation.

Mo<sub>2</sub>CT<sub>x</sub>/SiO<sub>2</sub> was dehydroxylated under a N<sub>2</sub> flow (20 mL min<sup>-1</sup>, with O<sub>2</sub> and moisture traps) at 500 °C for 12 h with a heating rate of 1 °C min<sup>-1</sup>. The sample was then cooled down under high vacuum (10<sup>-5</sup> mbar) for 1 h and handled in a glovebox (material referred to as Mo<sub>2</sub>CT<sub>x</sub>/SiO<sub>2-500</sub>). The surface density of hydroxyl groups of the support was determined by chemical titration using an excess of [Mg(CH<sub>2</sub>Ph)<sub>2</sub>(THF)<sub>2</sub>] as a reactant, while monitoring the extent of the reaction by <sup>1</sup>H NMR (d1 = 60s) using ferrocene as an internal standard<sup>36</sup>. Cu/Mo<sub>2</sub>CT<sub>x</sub>/SiO<sub>2</sub> was prepared via a surface organometallic chemistry approach using [Cu<sub>5</sub>(Mesityl)<sub>5</sub>] (Strem Chemicals)<sup>12,37</sup>. In a glovebox, Mo<sub>2</sub>CT<sub>x</sub>/SiO<sub>2-500</sub> (1 g, 0.47 mmol of ≡SiOH sites) was dispersed in 5 mL of dry toluene and contacted with a solution of [Cu<sub>5</sub>(Mesityl)<sub>5</sub>] (72 mg, 0.39 mmol of Cu) in 5 mL of toluene. The reaction mixture was stirred at 100 rpm for 3 h at room temperature. After the grafting, the solid was washed with

toluene ( $3 \times 5$  mL) and dried ( $10^{-5}$  mbar) at room temperature for 3 h. Before catalytic tests, the grafted material was reduced under  $H_2$  ( $50 \text{ mL min}^{-1}$ ) at  $500 \text{ }^\circ\text{C}$  for 2 h or 6 h (Cu/Mo<sub>2</sub>CT<sub>x</sub>/SiO<sub>2-2h</sub> and Cu/Mo<sub>2</sub>CT<sub>x</sub>/SiO<sub>2-6h</sub>, respectively). A reference Cu/SiO<sub>2-2h</sub> catalyst was prepared by the same procedure.

The industrial methanol synthesis catalyst (Alfa Aesar) contains 63.5 wt% CuO, 25 wt% ZnO, 10 wt% Al<sub>2</sub>O<sub>3</sub>, and 1.5 wt% MgO fume. In addition, a Cu-ZnO-Al<sub>2</sub>O<sub>3</sub> catalyst with 2.5 wt% Cu, 12.5 wt% ZnO, and 85.0 wt% Al<sub>2</sub>O<sub>3</sub> was synthesized by a conventional co-precipitation route<sup>5,7</sup>. More specifically, Cu(NO<sub>3</sub>)<sub>2</sub>·2.5H<sub>2</sub>O (183 mg, 0.8 mmol), Zn(NO<sub>3</sub>)<sub>2</sub>·6H<sub>2</sub>O (910 mg, 3.0 mmol), and Al(NO<sub>3</sub>)<sub>3</sub>·9H<sub>2</sub>O (6259 mg, 16.7 mmol) were dissolved in deionized water to make a 1 M solution. The solution was then titrated with 1 M Na<sub>2</sub>CO<sub>3</sub> to reach the pH of 8.0. The precipitate was filtered and washed with deionized water until pH 7.0 was reached. Subsequently, the precipitate was dried at  $90 \text{ }^\circ\text{C}$  overnight and calcined at  $350 \text{ }^\circ\text{C}$  for 12 h. The Cu-ZnO-Al<sub>2</sub>O<sub>3</sub> catalysts were reduced under  $H_2$  at  $250 \text{ }^\circ\text{C}$  for 3.5 h according to the published protocols<sup>3,5</sup> (denoted Cu-ZnO-Al<sub>2</sub>O<sub>3-com-250</sub> and Cu-ZnO-Al<sub>2</sub>O<sub>3-syn-250</sub>) or at  $500 \text{ }^\circ\text{C}$  for 6 h, according to the protocol for the synthesis of Cu/Mo<sub>2</sub>CT<sub>x</sub>/SiO<sub>2-6h</sub> in this study (denoted Cu-ZnO-Al<sub>2</sub>O<sub>3-com-250</sub> and Cu-ZnO-Al<sub>2</sub>O<sub>3-syn-250</sub>). The characterization of these catalysts is shown in Supplementary Figures 52–57.

### **Catalyst characterization**

The surface area and pore volume of the materials were determined by N<sub>2</sub> physisorption (Quantachrome NOVA 4000e) with the Brunauer-Emmet-Teller (BET) model (using the adsorption data) and Barrett-Joyner-Halenda (BJH) model (using the desorption data), respectively. Prior to the measurement, the samples were outgassed at  $250 \text{ }^\circ\text{C}$  for 2.5 h. The Mo and Cu loadings of the catalysts were determined by inductively coupled plasma optical

emission spectroscopy (ICP-OES) using an Agilent 5100 VDV after digestion in aqua regia. Fourier-Transform Infrared (FTIR) spectroscopy experiments were performed on self-supporting wafers using a Bruker Alpha spectrometer in transmission mode (24 scans, 4 cm<sup>-1</sup> resolution) under a N<sub>2</sub> atmosphere. Intensities were normalized to the Si-O-Si overtones of the silica support. Powder X-ray diffraction (XRD) data were collected on a PANalytical Empyrean X-ray diffractometer equipped with a Bragg-Brentano HD mirror operated at 45 kV and 40 mA using Cu K $\alpha$  radiation ( $\lambda = 1.5418 \text{ \AA}$ ). The materials were examined within the  $2\theta$  range of 5-90° using a step size of 0.0167°. The scan time per step was 3 s. X-ray photoelectron spectroscopy (XPS) measurements were conducted on a Sigma 2 instrument (Thermo Fisher Scientific) equipped with a UHV chamber (nonmonochromatic 200 W Al K $\alpha$  source, a hemispherical analyzer, and a seven-channel electron multiplier). The analyzer-to-source angle was 50°, whereas the emission angle was 0°. A pass energy of 50 and 25 eV was set for the survey and the narrow scans, respectively, and the C 1s peak of adventitious carbon was set at 284.8 eV to compensate for any charge-induced shift. An air-tight cell allowing to transfer specimens between the glovebox and the XPS instrument was used<sup>57</sup>.

X-ray absorption spectra at the Cu and Mo K-edge were measured at the SuperXAS beamline at the Swiss Light Source (SLS), operating in top-up mode at a 2.4-GeV electron energy and a current of 400 mA. Cu XAS spectra were collected at the K-edge using a Si (111) monochromator in transmission mode with continuous scanning between 8760 and 10290 eV with a step size of 0.1 eV. Mo XAS spectra were collected at the K-edge in fluorescence mode (Si drift detector) with continuous scanning between 19800 and 21150 eV with a step size of 0.25 eV. Calibration of the monochromator energy position was performed by setting the inflection point of a Cu or Mo foil spectrum recorded simultaneously with the sample to 8979 or 20000 eV for Cu or Mo K-edges, respectively. In a typical operando experiment, 4  $\pm$  0.05 mg of the sample (Cu/Mo<sub>2</sub>CT<sub>x</sub>/SiO<sub>2-0.5h</sub>) was packed into a quartz capillary reactor cell

(1.5 mm outer diameter, 0.02 mm wall thickness), which was connected with a pressurizable gas flow system. The catalysts went through the following steps: (i) heating to 500 °C under H<sub>2</sub> (1 bar, 10 mL min<sup>-1</sup>, 10 °C min<sup>-1</sup>) and holding for 5.5 h, (ii) cooling down to reaction temperature (230 °C) and pressurizing to 10 bar N<sub>2</sub>, and (iii) switching to a CO<sub>2</sub> hydrogenation atmosphere (H<sub>2</sub>/CO<sub>2</sub>/N<sub>2</sub> = 3/1/1, 10 mL min<sup>-1</sup>, 10 bar, space velocity = 150000 L kg<sup>-1</sup> h<sup>-1</sup>) and holding for 2 h. The outlet of the capillary reactor was kept at 150 °C and fed into a GC (CompactGC, Global Analyser Solutions, equipped with thermal conductivity and flame ionization detectors) with a data sampling interval of 7 min. The ex situ samples of air-sensitive CuMes/Mo<sub>2</sub>CT<sub>x</sub>/SiO<sub>2</sub> and Cu/Mo<sub>2</sub>CT<sub>x</sub>/SiO<sub>2-6h</sub> were sealed in the capillary in the glovebox and analyzed without exposure to air. Non-air-sensitive references were pressed into wafers with an optimized amount of sample mixed with cellulose and sealed in Kapton tape. The processing of the XAS data was performed with ProQEXAFS and the Athena software<sup>58,59</sup>, and the EXAFS fittings were conducted with the Artemis software<sup>59</sup>.

Transmission electron microscopy (TEM), scanning transmission electron microscopy (STEM) with a high-angle annular dark-field (HAADF) detection, and energy-dispersive X-ray (EDX) spectroscopy were carried out on an FEI Talos F200X transmission electron microscope. An aberration-corrected JEOL JEM-ARM300F Grand ARM scanning transmission electron microscope operated at 300 kV was also used with an air-tight sample holder. The microscope was equipped with the Dual EDS system (two large area SDD EDX detectors with 100 mm<sup>2</sup> active area; total solid angle: 1.6 sr). Gold grids were used. Scanning electron microscopy (SEM) measurements were performed on an FEI Magellan 400 FEG microscope. Prior to imaging, the samples were sputter-coated with a ca. 5 nm thick layer of PtPd (CCU-010 Metal Sputter Coater Safematic).

H<sub>2</sub> TPD and TPR experiments were performed using an AutoChem (Micromeritics) system with a thermal conductivity detector (TCD). In a typical H<sub>2</sub> TPD experiment, ca. 50 mg of the as-prepared material was loaded in air and reduced at 500 °C under H<sub>2</sub> flow (50 mL min<sup>-1</sup>) for the specified time. Subsequently, the sample was purged with Ar for 30 min at 500 °C and cooled down to -50 °C under Ar. The sample was then saturated in 5% H<sub>2</sub>/Ar flow for 30 min and purged with Ar for another 30 min. Finally, the sample was heated to 500 °C at 10 °C min<sup>-1</sup> under Ar flow and the desorbed H<sub>2</sub> was monitored with the TCD detector. For N<sub>2</sub>O titration measurements, specimens were first pretreated under H<sub>2</sub> at 500 °C, followed by purging and cooling down to 50 °C under Ar. The gas was then switched to 5% N<sub>2</sub>O/Ar for 60 min to oxidize the surface Cu<sup>0</sup> sites to Cu<sup>+</sup> and then reduced with 5% H<sub>2</sub>/Ar from room temperature to 500 °C (10 °C min<sup>-1</sup>). Similarly, the TPR experiments were carried out under 5% H<sub>2</sub>/Ar from room temperature to 500 °C after the sample was oxidized by 5% O<sub>2</sub>/He at room temperature.

DRIFTS measurements were performed using a Nicolet 6700 FTIR with a Praying Mantis (Harrick) high-pressure reaction chamber. A mercury cadmium telluride (MCT) detector was used. Catalysts were pelletized before the measurements and the spectra were recorded in the range of 4000-600 cm<sup>-1</sup> by averaging 64 scans with the resolution of 4 cm<sup>-1</sup>. For CO adsorption and desorption, the sample was loaded in air and pretreated with pure H<sub>2</sub> at 500 °C (50 mL min<sup>-1</sup>) for a specified period of time. After cooling down to room temperature, the specimen was exposed to 10% CO/N<sub>2</sub> flow (50 mL min<sup>-1</sup>) for 10 min, with spectra collected every two minutes. Then the CO flow was stopped and spectra were collected under flowing N<sub>2</sub> for 60 min. The temperature was then increased to 100 °C and 200 °C at a heating rate of 10 °C min<sup>-1</sup>. The background spectra were collected under N<sub>2</sub> at the corresponding temperatures. DRIFTS coupled with a GC-based gas analysis (CompactGC, Global Analyser

Solutions, equipped with thermal conductivity and flame ionization detectors) was used for the CO<sub>2</sub> hydrogenation reactions (i.e. in operando mode). After pretreatment with H<sub>2</sub> at 500 °C, the sample was cooled to 230 °C under N<sub>2</sub>. The DRIFT spectrum recorded under N<sub>2</sub> flow at 230 °C and 25 bar was used as the background spectrum. CO<sub>2</sub> hydrogenation was carried out at 230 °C and 25 bar using a gas mixture of H<sub>2</sub>/CO<sub>2</sub>/N<sub>2</sub> = 3/1/1 and the spectra were recorded every 2 min. The product was analyzed by the GC every 7 min. The transfer line was kept at 150 °C to prevent product condensation. The DRIFT spectra were also collected at different reaction pressures (1, 2, 3, 5, 10, 15, 20, and 25 bar) following a similar procedure.

The solid-state NMR experiments on <sup>1</sup>H and <sup>13</sup>C were recorded on a Bruker 400 MHz AVANCE III HD spectrometer with a 4 mm MAS triple resonance probe operating in double resonance mode with a magic angle spinning frequency of 10 kHz. The 35 kHz SPINAL64 decoupling was applied on the <sup>13</sup>C-channel during acquisition<sup>60</sup>. The chemical shift scale was calibrated using adamantane as an external secondary reference. Before the measurements, the catalysts were exposed to 5 bar <sup>1</sup>H<sub>2</sub>/<sup>13</sup>CO<sub>2</sub> (3/1) at 230 °C for 12 h in a batch reactor, followed by the evacuation of the gas phase at room temperature under high vacuum (10<sup>-5</sup> mbar).

### **CO<sub>2</sub> hydrogenation reactions**

The CO<sub>2</sub> hydrogenation reactions were performed in a fixed-bed, tubular reactor (304.8 mm total length, 9.1 mm internal diameter, Hastelloy X, Microactivity Effi, PID Eng&Tech)<sup>61</sup>. In a typical experiment, the catalyst (100 mg) was first pretreated under H<sub>2</sub> at 500 °C for a specific time. The reaction was performed at 230 °C under 25 bar. The gas flow of H<sub>2</sub>/CO<sub>2</sub>/N<sub>2</sub> (3/1/1) (N<sub>2</sub> as internal standard) was passed through the catalyst bed and the

products were analyzed online by a GC (PerkinElmer Clarus 580) equipped with thermal conductivity and flame ionization detectors, and a methanizer. Different contact times (space velocities) were probed by changing the gas flow rate from 100 to 15 NmL min<sup>-1</sup>. Finally, activity data were collected at the initial flow rate of 100 NmL min<sup>-1</sup> to check for potential deactivation of the catalyst. The formation rate, CO<sub>2</sub> conversion, and methanol selectivity were calculated using the following equations:

$$F_{x,out} [\text{mol h}^{-1}] = \frac{C_{x,out} F_{N_2,in}}{C_{N_2,out}} \quad (1)$$

$$r_x [\text{g h}^{-1} \text{g}_{\text{Cu}}^{-1}] = \frac{F_{x,out}}{m_{\text{Cu}}} \times MW_x \quad (2)$$

$$X_{\text{CO}_2} = \frac{\sum_{i=1}^n F_{x,out}}{F_{\text{CO}_2,in}} \quad (3)$$

$$S_{\text{MeOH}} = \frac{F_{\text{MeOH,out}}}{\sum_{i=1}^n F_{x,out}} \quad (4)$$

where  $F_{x,out}$  is the outlet flow rate of methanol or CO [mol h<sup>-1</sup>];  $C_{x,out}$  is the outlet gas fraction of species  $x$ ;  $F_{x,in}$  is the inlet flow rate of species  $x$  [mol h<sup>-1</sup>];  $r_x$  is the formation rate of methanol or CO [g h<sup>-1</sup> g<sub>Cu</sub><sup>-1</sup>];  $m_{\text{Cu}}$  is the mass of Cu used in the reaction [g];  $MW_x$  is the molecular weight of methanol or CO [g mol<sup>-1</sup>];  $X_{\text{CO}_2}$  is the conversion of CO<sub>2</sub>;  $S_{\text{MeOH}}$  is the selectivity to methanol. Intrinsic formation rates and selectivities were extrapolated using a second-order polynomial fit of the experimental data. At least three experimental data points were averaged for each presented data point.

## Computational Details

The periodic density functional theory (DFT) calculations were carried out with the Vienna Ab Initio Simulation Package (VASP) code<sup>62–64</sup>. Projector-augmented-wave (PAW) pseudopotentials were used to describe the interactions between valence electrons and ion cores, while a discrete plane wave (PW) basis set with a cutoff of 500 eV was used to treat

valence electrons<sup>65</sup>. All geometries, adsorption energies, vibrational frequencies and Bader charges were calculated via the Generalized Gradient Approximation (GGA) including dispersion corrections by means of the BEEF-vdW density functional<sup>52</sup>. A  $3 \times 3$  unit cell was used to construct a Mo<sub>2</sub>C (001) surface slab using two Mo layers, with one at the top and one at the bottom of the slab, and one middle carbon layer. The Cu (111) surface model comprising a periodic  $3 \times 3$  seven-layer slab and a Cu<sub>2</sub>O (111) surface comprising a periodic  $3 \times 3$  five-layer slab were constructed. 15 Å of vacuum was added in the direction perpendicular to the surface for all the models. Dipole correction was considered in all the calculations in order to correct the errors introduced by the periodic boundary conditions. Self-Consistent Field (SCF) calculations of the electronic structure were considered converged when the electronic energy change between two steps was below  $10^{-5}$  eV. All minima geometries were optimized using an energy-based conjugate gradient algorithm until the forces acting on each atom were converged below 0.01 eV/Å. The energy of isolated molecules was determined by a single-point calculation placing each species in a box with dimensions 15 Å  $\times$  15 Å  $\times$  15 Å. The Nudge Elastic Band (NEB) method<sup>66</sup> with 8 intermediate images was used to locate transition states (TS). The transition-state structures were further refined using a Newton-based algorithm using the same convergence criteria as for the minima. All reported energy values in the text correspond to electronic energies. In all the profiles, the values have been calculated with respect to the energy of the initial reactants (in kJ mol<sup>-1</sup>).

**DATA AVAILABILITY** All data is available from the authors upon reasonable request. Calculated DFT structures and energies are freely available at <https://doi.org/10.19061/iochem-bd-6-100><sup>67</sup>.

## **Acknowledgments**



We acknowledge funding from the European Union's Horizon 2020 research and innovation program (grant agreement 800419, H.Z.), ETH Zürich (grant agreement ETH-40 17-2, Z.C.), Spanish "Ministerio de Innovación y Universidades" (grant agreement PRE2019-089647, A.V.L.), InnoSuisse - SCCER Heat and Electricity Storage (grant agreement KTI 1155002545, E.L.), ETH Zürich (grant agreement ETH-44 16-2, A.T.), European Research Council (ERC, grant agreement 819573, E.L.), ETH Postdoctoral Fellowship Program and the Marie Curie Actions for People COFUND (grant agreement 18-1 FEL 51, D.M.), Spanish MEC and the European Social Fund (grant agreement RyC-2016-19930, A.C.-V.) and Spanish "Ministerio de Innovación y Universidades" (grant agreement PGC2018-100818-A-I00, A.C.-V.). The funders had no role in study design, data collection and analysis, decision to publish or preparation of the manuscript. The authors thank ScopeM (ETH Zürich) for the use of their electron microscopy facilities and the Laboratory of Surface Science and Technology (LSST, ETH Zürich) for the use of their XPS facilities. We also acknowledge PSI Super-XAS for beamtime and thank Dr. Olga Safonova for assistance.

### **Author contributions**

A.F. conceived the research project. H.Z. planned the experimental work. Z.C, H.Z., and D.A.K. prepared MXene-based supports. H.Z. and E.L. prepared the Cu grafted materials. H.Z. prepared, characterized and tested the catalysts, and analyzed the data. E.L. and D.M. performed solid-state NMR experiments. A.T. and E.W. performed XPS and HR-TEM imaging, respectively. A.K. and F.D. performed ICP analysis. Z.C. and P.M.A. performed XAS experiments. P.M.A. supervised XAS experiments. A.V.L., E.D.L. and A.C.-V. designed and performed DFT calculations. A.C.-V. supervised DFT calculations. C.C., A.F. and C.R.M. coordinated the research. The data were discussed among all co-authors. H.Z. and A.F. wrote the paper with contributions from all authors.

### **Competing interests**

The authors declare no competing interests.

## Figure Legends/Captions

**Fig. 1. Synthesis, characterization, and activity of Cu/Mo<sub>2</sub>CT<sub>x</sub>/SiO<sub>2</sub>.** **a**, Schematic of the synthesis of Cu/Mo<sub>2</sub>CT<sub>x</sub>/SiO<sub>2-500</sub> with highly dispersed Cu sites in interaction with partially reduced Mo<sub>2</sub>CT<sub>x</sub> nanosheets. **b**, IR spectra of Mo<sub>2</sub>CT<sub>x</sub>/SiO<sub>2-500</sub> before (black) and after grafting of CuMes (red), and after treatment in H<sub>2</sub> at 500 °C for 2 h (blue). **c**, HAADF-EDX of Cu/Mo<sub>2</sub>CT<sub>x</sub>/SiO<sub>2-2h</sub> (scale bar is 50 nm). **d-f**, High-resolution HAADF-STEM of Cu/Mo<sub>2</sub>CT<sub>x</sub>/SiO<sub>2-2h</sub> recorded without exposure of the specimen to air (arrows in **d** indicate Mo vacancies in Mo<sub>2</sub>CT<sub>x</sub>; circles in **e** point at few-atoms-small clusters and single Cu atoms; arrows in **f** indicate the edges of Mo<sub>2</sub>CT<sub>x</sub> nanosheets decorated with Cu atoms). **g**, Comparison of intrinsic formation rates of CH<sub>3</sub>OH and CO of the catalysts tested (230 °C, 25 bar, H<sub>2</sub>/CO<sub>2</sub>/N<sub>2</sub> = 3/1/1) obtained by extrapolation to zero conversion (zero contact time, see Supplementary Figures 6 and 12) together with the selectivities for CH<sub>3</sub>OH and CO, specified above the respective bars. The Cu-ZnO-Al<sub>2</sub>O<sub>3-com</sub> denotes the commercial Cu-ZnO-Al<sub>2</sub>O<sub>3</sub> catalyst (pre-treated in H<sub>2</sub> at 250 °C for 3.5 h before the catalytic test). **h**, Dependence of CH<sub>3</sub>OH selectivity on CO<sub>2</sub> conversion by varying the contact time (see Supplementary Figure 6). **i**, Formation rates of CH<sub>3</sub>OH and CO with a contact time of 0.06 s g mL<sup>-1</sup> on Cu/Mo<sub>2</sub>CT<sub>x</sub>/SiO<sub>2</sub> pretreated in H<sub>2</sub> for varying reduction times (2–12 h) at 500 °C. The dashed lines correspond to the catalyst pretreated in H<sub>2</sub> for 2 h followed by treatment in N<sub>2</sub> for an additional 2 h at 500 °C.

**Fig. 2. Characterization and DFT models of the catalysts.** **a**, Cu L<sub>3</sub>VV Auger spectra (see Supplementary Table 5 for details). **b**, Temperature-programmed reduction under 5% H<sub>2</sub>/Ar after oxidation of the specimen by 5% O<sub>2</sub>/He at room temperature. **c**, H<sub>2</sub> temperature-programmed hydrogen desorption after saturation in 5% H<sub>2</sub>/Ar. **d**, DRIFTS spectra after

desorption of CO at different temperatures (see Supplementary Figure 34 for the spectra in Kubelka-Munk units). **e–g**, Optimized structures for the H adsorption on Cu/2D-Mo<sub>2</sub>C (**e**), Cu<sub>4</sub>/2D-Mo<sub>2</sub>C (**f**), and Cu/2D-Mo<sub>2</sub>C-0.67 O ML (**g**), respectively. **h–i**, Optimized structures for the CO adsorbed on Models 4 (**h**) and 5 (**i**) with respective C–O bond distances and CO adsorption energies ( $E_{\text{ads}}$ ). The interpolated oxidation states are shown for the Cu atoms (Supplementary Figure 39).

**Fig. 3. Characterization and evolution of reactive intermediates.** **a**, Evolution of the DRIFTS spectra over Cu/Mo<sub>2</sub>CT<sub>x</sub>/SiO<sub>2-2h</sub> (230 °C, 25 bar, H<sub>2</sub>/CO<sub>2</sub>/N<sub>2</sub> = 3/1/1) with TOS. **b**, Operando DRIFTS GC data of CO<sub>2</sub> hydrogenation over Cu/SiO<sub>2-2h</sub> and Cu/Mo<sub>2</sub>CT<sub>x</sub>/SiO<sub>2-2h</sub> and corresponding evolution of the reaction rate. Peaks at 2857 and 2959 cm<sup>-1</sup> were used to assess the intensity of formate and methoxy species, respectively. **c**, Solid-state cross-polarization magic angle spinning (CP-MAS) <sup>13</sup>C NMR spectra of Cu/Mo<sub>2</sub>CT<sub>x</sub>/SiO<sub>2-2h</sub> and Mo<sub>2</sub>CT<sub>x</sub>/SiO<sub>2-2h</sub> after exposure of H<sub>2</sub>/<sup>13</sup>CO<sub>2</sub> (ca. 3/1) for 12 h at 230 °C and 5 bar.

**Fig. 4. DFT-computed energy profiles.** Considered reactions are CO<sub>2</sub> and 2H<sub>2</sub>, or CO<sub>2</sub> and 1H<sub>2</sub>, to form methanol and O\* (blue trace), or CO and H<sub>2</sub>O (magenta trace, RWGS reaction), respectively. Energies are shown with respect to the initial reactants in kJ mol<sup>-1</sup> ( $E_{\text{rel}}$ ). Only selected intermediates and transition states (TS) are presented with their respective energies shown in parenthesis. See Supplementary Figure 44 for the structures of other intermediates and transition states and for their energies.

## References

1. Goeppert, A., Czaun, M., Jones, J.-P., Surya Prakash, G. K. & Olah, G. A. Recycling of carbon dioxide to methanol and derived products – closing the loop. *Chem. Soc. Rev.* **43**, 7995–8048 (2014).
2. Olah, G. A. Beyond Oil and Gas: The Methanol Economy. *Angew. Chem. Int. Ed.* **44**, 2636–2639 (2005).

- Behrens, M. *et al.* The Active Site of Methanol Synthesis over Cu/ZnO/Al<sub>2</sub>O<sub>3</sub> Industrial Catalysts. *Science* **336**, 893–897 (2012).
- Lunkenbein, T., Schumann, J., Behrens, M., Schlögl, R. & Willinger, M. G. Formation of a ZnO Overlayer in Industrial Cu/ZnO/Al<sub>2</sub>O<sub>3</sub> Catalysts Induced by Strong Metal–Support Interactions. *Angew. Chem. Int. Ed.* **54**, 4544–4548 (2015).
- Lee, J. S., Lee, K. H., Lee, S. Y. & Kim, Y. G. A comparative study of methanol synthesis from CO<sub>2</sub>/H<sub>2</sub> and CO/H<sub>2</sub> over a Cu/ZnO/Al<sub>2</sub>O<sub>3</sub> catalyst. *J. Catal.* **144**, 414–424 (1993).
- Kattel, S., Ramírez, P. J., Chen, J. G., Rodriguez, J. A. & Liu, P. Active sites for CO<sub>2</sub> hydrogenation to methanol on Cu/ZnO catalysts. *Science* **355**, 1296–1299 (2017).
- Martin, O. & Pérez-Ramírez, J. New and revisited insights into the promotion of methanol synthesis catalysts by CO<sub>2</sub>. *Catal. Sci. Technol.* **3**, 3343–3352 (2013).
- Rozovskii, A. Y. & Lin, G. I. Fundamentals of methanol synthesis and decomposition. *Top. Catal.* **22**, 137–150 (2003).
- Zhang, Y., Sun, Q., Deng, J., Wu, D. & Chen, S. A high activity Cu/ZnO/Al<sub>2</sub>O<sub>3</sub> catalyst for methanol synthesis: Preparation and catalytic properties. *Appl. Catal. Gen.* **158**, 105–120 (1997).
- Klier, K., Chatikavanij, V., Herman, R. G. & Simmons, G. W. Catalytic synthesis of methanol from CO/H<sub>2</sub>: IV. The effects of carbon dioxide. *J. Catal.* **74**, 343–360 (1982).
- Ruland, H. *et al.* CO<sub>2</sub> Hydrogenation with Cu/ZnO/Al<sub>2</sub>O<sub>3</sub>: A Benchmark Study. *ChemCatChem* **12**, 3216–3222 (2020).
- Lam, E. *et al.* Isolated Zr Surface Sites on Silica Promote Hydrogenation of CO<sub>2</sub> to CH<sub>3</sub>OH in Supported Cu Catalysts. *J. Am. Chem. Soc.* **140**, 10530–10535 (2018).
- Larmier, K. *et al.* CO<sub>2</sub>-to-Methanol Hydrogenation on Zirconia-Supported Copper Nanoparticles: Reaction Intermediates and the Role of the Metal–Support Interface. *Angew. Chem. Int. Ed.* **56**, 2318–2323 (2017).
- Kattel, S., Yan, B., Yang, Y., Chen, J. G. & Liu, P. Optimizing Binding Energies of Key Intermediates for CO<sub>2</sub> Hydrogenation to Methanol over Oxide-Supported Copper. *J. Am. Chem. Soc.* **138**, 12440–12450 (2016).
- Noh, G. *et al.* Selective Hydrogenation of CO<sub>2</sub> to CH<sub>3</sub>OH on Supported Cu Nanoparticles Promoted by Isolated Ti<sup>IV</sup> Surface Sites on SiO<sub>2</sub>. *ChemSusChem* **12**, 968–972 (2019).
- Graciani, J. *et al.* Highly active copper-ceria and copper-ceria-titania catalysts for methanol synthesis from CO<sub>2</sub>. *Science* **345**, 546–550 (2014).

17. Lam, E. *et al.* CO<sub>2</sub> Hydrogenation on Cu/Al<sub>2</sub>O<sub>3</sub>: Role of the Metal/Support Interface in Driving Activity and Selectivity of a Bifunctional Catalyst. *Angew. Chem. Int. Ed.* **58**, 13989–13996 (2019).
18. Studt, F. *et al.* The Mechanism of CO and CO<sub>2</sub> Hydrogenation to Methanol over Cu-Based Catalysts. *ChemCatChem* **7**, 1105–1111 (2015).
19. Docherty, S. R. & Copéret, C. Deciphering Metal–Oxide and Metal–Metal Interplay via Surface Organometallic Chemistry: A Case Study with CO<sub>2</sub> Hydrogenation to Methanol. *J. Am. Chem. Soc.* **143**, 6767–6780 (2021).
20. Yao, S. *et al.* Atomic-layered Au clusters on  $\alpha$ -MoC as catalysts for the low-temperature water-gas shift reaction. *Science* **357**, 389–393 (2017).
21. Lin, L. *et al.* Low-temperature hydrogen production from water and methanol using Pt/ $\alpha$ -MoC catalysts. *Nature* **544**, 80–83 (2017).
22. Dong, J., Fu, Q., Jiang, Z., Mei, B. & Bao, X. Carbide-Supported Au Catalysts for Water–Gas Shift Reactions: A New Territory for the Strong Metal–Support Interaction Effect. *J. Am. Chem. Soc.* **140**, 13808–13816 (2018).
23. Zhang, X. *et al.* Highly Dispersed Copper over  $\beta$ -Mo<sub>2</sub>C as an Efficient and Stable Catalyst for the Reverse Water Gas Shift (RWGS) Reaction. *ACS Catal.* **7**, 912–918 (2017).
24. Posada-Pérez, S. *et al.* The conversion of CO<sub>2</sub> to methanol on orthorhombic  $\beta$ -Mo<sub>2</sub>C and Cu/ $\beta$ -Mo<sub>2</sub>C catalysts: mechanism for admetal induced change in the selectivity and activity. *Catal. Sci. Technol.* **6**, 6766–6777 (2016).
25. Anasori, B., Lukatskaya, M. R. & Gogotsi, Y. 2D metal carbides and nitrides (MXenes) for energy storage. *Nat. Rev. Mater.* **2**, 16098 (2017).
26. Sarycheva, A. *et al.* 2D titanium carbide (MXene) for wireless communication. *Sci. Adv.* **4**, eaau0920 (2018).
27. Naguib, M. *et al.* Two-Dimensional Nanocrystals Produced by Exfoliation of Ti<sub>3</sub>AlC<sub>2</sub>. *Adv. Mater.* **23**, 4248–4253 (2011).
28. Deeva, E. B. *et al.* In Situ XANES/XRD Study of the Structural Stability of Two-Dimensional Molybdenum Carbide Mo<sub>2</sub>CT<sub>x</sub> Implications for the Catalytic Activity in the Water–Gas Shift Reaction. *Chem. Mater.* **31**, 4505–4513 (2019).
29. Diao, J. *et al.* Ti<sub>3</sub>C<sub>2</sub>T<sub>x</sub> MXene Catalyzed Ethylbenzene Dehydrogenation: Active Sites and Mechanism Exploration from both Experimental and Theoretical Aspects. *ACS Catal.* **8**, 10051–10057 (2018).

30. Kurlov, A. *et al.* Exploiting two-dimensional morphology of molybdenum oxycarbide to enable efficient catalytic dry reforming of methane. *Nat. Commun.* **11**, 4920 (2020).
31. Li, Z. *et al.* Reactive metal–support interactions at moderate temperature in two-dimensional niobium-carbide-supported platinum catalysts. *Nat. Catal.* **1**, 349–355 (2018).
32. Li, Z. *et al.* Two-dimensional transition metal carbides as supports for tuning the chemistry of catalytic nanoparticles. *Nat. Commun.* **9**, 5258 (2018).
33. Lang, Z. *et al.* MXene Surface Terminations Enable Strong Metal–Support Interactions for Efficient Methanol Oxidation on Palladium. *ACS Appl. Mater. Interfaces* **12**, 2400–2406 (2020).
34. Zhao, D. *et al.* MXene (Ti<sub>3</sub>C<sub>2</sub>) Vacancy-Confined Single-Atom Catalyst for Efficient Functionalization of CO<sub>2</sub>. *J. Am. Chem. Soc.* **141**, 4086–4093 (2019).
35. Morales-García, Á., Fernández-Fernández, A., Viñes, F. & Illas, F. CO<sub>2</sub> abatement using two-dimensional MXene carbides. *J. Mater. Chem. A* **6**, 3381–3385 (2018).
36. Copéret, C. *et al.* Surface Organometallic and Coordination Chemistry toward Single-Site Heterogeneous Catalysts: Strategies, Methods, Structures, and Activities. *Chem. Rev.* **116**, 323–421 (2016).
37. Fedorov, A., Liu, H.-J., Lo, H.-K. & Copéret, C. Silica-Supported Cu Nanoparticle Catalysts for Alkyne Semihydrogenation: Effect of Ligands on Rates and Selectivity. *J. Am. Chem. Soc.* **138**, 16502–16507 (2016).
38. Zhang, J. *et al.* Single platinum atoms immobilized on an MXene as an efficient catalyst for the hydrogen evolution reaction. *Nat. Catal.* **1**, 985 (2018).
39. Lauritsen, J. V. *et al.* Location and coordination of promoter atoms in Co- and Ni-promoted MoS<sub>2</sub>-based hydrotreating catalysts. *J. Catal.* **249**, 220–233 (2007).
40. Zhu, G. *et al.* Enhanced CO<sub>2</sub> electroreduction on armchair graphene nanoribbons edge-decorated with copper. *Nano Res.* **10**, 1641–1650 (2017).
41. Ro, I. *et al.* Role of the Cu-ZrO<sub>2</sub> Interfacial Sites for Conversion of Ethanol to Ethyl Acetate and Synthesis of Methanol from CO<sub>2</sub> and H<sub>2</sub>. *ACS Catal.* **6**, 7040–7050 (2016).
42. Halim, J. *et al.* Synthesis and Characterization of 2D Molybdenum Carbide (MXene). *Adv. Funct. Mater.* **26**, 3118–3127 (2016).
43. Cramer, S. P., Eccles, T. K., Kutzler, F. W., Hodgson, K. O. & Mortenson, L. E. Molybdenum x-ray absorption edge spectra. The chemical state of molybdenum in nitrogenase. *J. Am. Chem. Soc.* **98**, 1287–1288 (1976).

44. Chen, A. *et al.* Structure of the catalytically active copper–ceria interfacial perimeter. *Nat. Catal.* **2**, 334–341 (2019).
45. Newton, M. A. *et al.* Unwanted effects of X-rays in surface grafted copper(II) organometallics and copper exchanged zeolites, how they manifest, and what can be done about them. *Phys. Chem. Chem. Phys.* **22**, 6826–6837 (2020).
46. Frenkel, A. I. Solving the structure of nanoparticles by multiple-scattering EXAFS analysis. *J. Synchrotron Radiat.* **6**, 293–295 (1999).
47. de Jong, K. P., Geus, J. W. & Joziassse, J. An infrared spectroscopic study of the adsorption of carbon monoxide on silica-supported copper particles. *Appl. Surf. Sci.* **6**, 273–287 (1980).
48. Smith, M. L., Kumar, N. & Spivey, J. J. CO Adsorption Behavior of Cu/SiO<sub>2</sub>, Co/SiO<sub>2</sub>, and CuCo/SiO<sub>2</sub> Catalysts Studied by in Situ DRIFTS. *J. Phys. Chem. C* **116**, 7931–7939 (2012).
49. Subramanian, N. D. *et al.* A DRIFTS study of CO adsorption and hydrogenation on Cu-based core–shell nanoparticles. *Catal. Sci. Technol.* **2**, 621 (2012).
50. Cox, D. F. & Schulz, K. H. Interaction of CO with Cu<sup>+</sup> cations: CO adsorption on Cu<sub>2</sub>O (100). *Surf. Sci.* **249**, 138–148 (1991).
51. Fisher, I. A. & Bell, A. T. In situ infrared study of methanol synthesis from H<sub>2</sub>/CO over Cu/SiO<sub>2</sub> and Cu/ZrO<sub>2</sub>/SiO<sub>2</sub>. *J. Catal.* **178**, 153–173 (1998).
52. Wellendorff, J. *et al.* Density functionals for surface science: Exchange–correlation model development with Bayesian error estimation. *Phys. Rev. B* **85**, 235149 (2012).
53. Baiker, A., Kilo, M., Maciejewski, M., Menzi, S. & Wokaun, A. Hydrogenation of CO<sub>2</sub> Over Copper, Silver and Gold/Zirconia Catalysts: Comparative Study of Catalyst Properties and Reaction Pathways. in *Studies in Surface Science and Catalysis* (eds. Guenzi, L., Solymosi, F. & Tétényi, P.) vol. 75 1257–1272 (Elsevier, 1993).
54. Fehr, S. M. & Krossing, I. Spectroscopic Signatures of Pressurized Carbon Dioxide in Diffuse Reflectance Infrared Spectroscopy of Heterogeneous Catalysts. *ChemCatChem* **12**, 2622–2629 (2020).
55. Quan, J. *et al.* Vibration-driven reaction of CO<sub>2</sub> on Cu surfaces via Eley–Rideal-type mechanism. *Nat. Chem.* **11**, 722–729 (2019).
56. Baxter, R. J. & Hu, P. Insight into why the Langmuir–Hinshelwood mechanism is generally preferred. *J. Chem. Phys.* **116**, 4379–4381 (2002).

57. Cossu, G., Rossi, A., Arcifa, A. & Spencer, N. D. Development and application of a cost-effective transfer cell for X-ray photoelectron spectroscopy. in *Incontro di Spettroscopia Analitica ISA* (2018).
58. Clark, A. H., Imbao, J., Frahm, R. & Nachtegaal, M. ProQEXAFS: a highly optimized parallelized rapid processing software for QEXAFS data. *J. Synchrotron Radiat.* **27**, 551–557 (2020).
59. Ravel, B. & Newville, M. ATHENA, ARTEMIS, HEPHAESTUS: data analysis for X-ray absorption spectroscopy using IFEFFIT. *J. Synchrotron Radiat.* **12**, 537–541 (2005).
60. Fung, B. M., Khitrin, A. K. & Ermolaev, K. An Improved Broadband Decoupling Sequence for Liquid Crystals and Solids. *J. Magn. Reson.* **142**, 97–101 (2000).
61. Tsoukalou, A. *et al.* Structural Evolution and Dynamics of an In<sub>2</sub>O<sub>3</sub> Catalyst for CO<sub>2</sub> Hydrogenation to Methanol: An Operando XAS-XRD and In Situ TEM Study. *J. Am. Chem. Soc.* **141**, 13497–13505 (2019).
62. Kresse, G. & Hafner, J. Ab initio molecular dynamics for liquid metals. *Phys. Rev. B* **47**, 558–561 (1993).
63. Kresse, G. & Hafner, J. Ab initio molecular-dynamics simulation of the liquid-metal--amorphous-semiconductor transition in germanium. *Phys. Rev. B* **49**, 14251–14269 (1994).
64. Kresse, G. & Furthmüller, J. Efficiency of ab-initio total energy calculations for metals and semiconductors using a plane-wave basis set. *Comput. Mater. Sci.* **6**, 15–50 (1996).
65. Blöchl, P. E. Projector augmented-wave method. *Phys. Rev. B* **50**, 17953–17979 (1994).
66. Jonsson, H., Mills, G. & Jacobsen, K. Nudged elastic band method for finding minimum energy paths of transitions. in *Classical and Quantum Dynamics in Condensed Phase Simulations* 385–404 (1998).  
doi:10.1142/9789812839664\_0016.
67. Álvarez-Moreno, M., de Graaf, C., Lopez, N., Maseras, F., Poblet, J. M. & Bo, C. *J. Chem. Inf. Model.* **55**, 95–103 (2015).